This is a postprint version of the article published as:
Su, M., Liu, J., Zhou, S., Miao, J. & Kim, M.K. Dynamic prediction of the pre-dehumidification of a radiant floor cooling and displacement ventilation system based on computational fluid dynamics and a back-propagation neural network: A case study of an office room. Indoor and Built Environment, 2022, 31 (10), 2386-2410

Dynamic prediction of the pre-dehumidification of a radiant floor cooling and displacement ventilation system based on CFD and a BP neural network: A case study of an office room

Meng Su[1], Jiying Liu[1,2,*], Shiyu Zhou[1], Jikui Miao[3], Moon Keun Kim[4]

[1]School of Thermal Engineering, Shandong Jianzhu University, Jinan 250101, China
[2]Built Environment Design and Research Institute, Shandong GRAD Group, Dezhou 253000, China
[3]School of Architecture and Urban Planning, Shandong Jianzhu University, Jinan 250101, China
[4]Department of Civil Engineering and Energy Technology, Oslo Metropolitan University, Oslo, N-0130, Norway

* Corresponding Author.
Dr. Jiying Liu, School of Thermal Engineering, Shandong Jianzhu University, Jinan 250101, China.
Email:jxl83@sdjzu.edu.cn.

Abstract: This study was carried out to solve the problem of condensation in radiant floor cooling (RFC) systems. Computational fluid dynamics (CFD) simulation and back-propagation (BP) neural network prediction were employed to conduct thorough research to predict the effects of the displacement ventilation (DV) dehumidification phase in an office building located in Jinan, China. The effects of the air supply temperature (T_{as}), air supply flow rate (V_{as}), air supply humidity ratio (H_{as}), floor temperature (T_{floor}), initial indoor temperature (T_{ini}) and relative humidity (H_{ini}) on the duration and energy consumption of pre-dehumidification were investigated. The big data show the air dew point temperature (T_{ad}) produced the most significant effect on the pre-dehumidification duration and energy consumption, while T_{as} would cause the least significant effect. With the decrease of T_{ad}, the pre-dehumidification duration and energy consumption were respectively decreased by 59.1% and 44.2%. Furthermore, with the variation of V_{as}, the energy consumption exhibited a fluctuating trend. This study provides a novel and effective method to assess the pre-dehumidification control of radiant floor surfaces by considering different initial indoor conditions and air supply parameters.

Keywords
floor condensation, radiant floor cooling, displacement ventilation, CFD, pre-dehumidification, BP neural network

Introduction

Due to the improvement of the living environment and the development of urbanization, building energy consumption in urban areas is rapidly increasing.[1] China has been the largest carbon emitter and energy consumer country in the world since 2011. Generally speaking, building energy consumption is mainly used for lighting, electrical equipment and heating, ventilation and air conditioning (HVAC) systems, of which about 50% is mainly from the traditional HVAC system.[2,3] Therefore, the application of energy-saving technology in HVAC systems is a necessary means to slow down the trend of energy consumption.

In recent years, radiant cooling systems have risen in popularity due to their energy-saving potential and high thermal comfort level as compared with conventional air conditioning systems.[4-7] However, radiant cooling systems have limited use in hot and humid climates. Driven by hot pressure, high-temperature and high-humidity air enter indoors via gaps in buildings. Moreover, the indoor air humidity would increase due to the high infiltration rates and moisture generation by the occupants, resulting in an increase in the indoor air dew point temperature (T_{ad}).[8] These factors would increase the risk of condensation on the surface of radiant panels,[9-10] and decrease the comfort of the indoor environment, thereby limiting the widespread use of radiant cooling systems.

The occurrence of condensation is the main drawback of radiant cooling systems. Condensation occurs when the temperature of the radiant panel is lower than the dew point temperature of the air; thus, the use of radiant cooling systems in humid environments is a substantial challenge. Therefore, the prevention of radiant panel condensation in radiant cooling systems is one of the main areas of investigation. Current studies on radiant cooling system condensation prevention primarily focus on three areas, namely the basic theory of radiant cooling condensation,[11-13] condensation prevention strategies[14-16] and the improvement of the radiant panel to prevent condensation.[17-19]

However, as compared with radiant ceiling cooling systems,[20,21] which are mostly applied in hot and humid climates,[22] radiant floor cooling (RFC) systems have only been evaluated in a limited number of studies due to the potential contradictions of maintaining sufficient cooling capacity while preventing the condensation and local discomfort caused by lower floor temperatures and larger vertical temperature differences.[23] Tang et al.[24] theoretically and experimentally studied the condensation rate of radiant cooling surfaces at different locations of wet air (the floor, wall and ceiling); the results showed that with the same air state and surface temperature, the condensation rate on the radiant ceiling was about 3.5 times higher than that on the radiant floor, and about 25% higher than that on the radiant wall. Consequently, the condensation risk of the radiant floor is much lower than that of the radiant wall or the ceiling. Lim et al.[25] showed that to maintain the indoor temperature, controlling the water temperature is better than controlling the water flow. Due to the use of this control method, the floor temperature was able to be maintained above 21°C, the surface dew was not formed, the vertical temperature difference was less than 1.9°C and the thermal comfort was good. Jeong et al.[26] proposed a strategy for the configuration and arrangement of an RFC using an individual cooling source, which was derived for application to residential buildings in regions with a hot and humid summer climate, such as Korea. The results revealed that during most of the measurement period, the indoor temperature remained at the indoor set point temperature, and the floor surface temperature was higher than the indoor dew point temperature. Therefore, RFC combined with dehumidification and refrigeration equipment can meet the refrigeration and dew prevention requirements of multi-zone homes. In addition, the dehumidification of fresh or indoor air by an independent air supply dehumidification device can reduce the moisture content of the indoor air and effectively reduce the risk of condensation at the end of the radiant cooling.[27]

When comparing ventilation strategies,[28,29] air quality and thermal comfort are usually used as evaluation criteria. Triggered by the advent of the energy crisis, emphasis has been placed on the energy efficiency of office buildings. Space conditioning contributes substantially to energy consumption in office buildings. To reduce this high energy cost, office building design has shifted toward high levels of insulation and airtightness, as well as a minimal ventilation rate. However, this has led to the deterioration of indoor air quality. Therefore, further investigation of the indoor environment quality in ventilated office spaces should be oriented toward a holistic evaluation of thermal comfort, indoor air quality and energy efficiency.[30]

There are two methods commonly used to supply the air in a room, namely mixed ventilation (MV) and displacement ventilation (DV). In MV, the air is normally supplied at a high level over the ceiling and then deflected down into the occupied zone by the opposite walls, thereby causing a mixing of the air jet with the room air. In DV, the air is supplied at a low level, usually over the floor, and then rises due to buoyancy before it is extracted at a high level.[31] Among these two ventilation strategies, DV is regarded as one of the most interesting solutions because it can provide a high level of air quality at the breathing level. Xing et al.[32] conducted a computational fluid dynamic (CFD) simulation and reported that higher air quality can be obtained in the working area of a room with DV as compared with a room with MV. By exploiting buoyancy forces in the room, DV could generate a stratified flow pattern: the warm and polluted air is concentrated in the upper part of the room, while the cool and clean air remains in the lower part of the room where the occupants are located, while also reducing energy consumption by 20% to 30%. Although some relevant studies have been conducted on the combination of RFC and DV systems, most have focused on indoor thermal comfort.[33-35] The research on the pre-dehumidification of this composite system based on CFD modelling is limited. While experimental studies are reliable, they are characterized by the disadvantages of a high consumption of time, manpower and financial resources. Recently, neural network models have been successfully applied to buildings and air conditioning systems,[36-38] but numerous studies have been based on TRNSYS software and neural networks to conduct forecast analyses. Because the air distribution in the room directly affects the effects of ventilation and air conditioning, the use of TRNSYS cannot yield the detailed distribution of the air in a space. Compared with experimental studies, CFD is characterized by lower costs, and compared with TRNSYS analysis, the detailed situation of the air distribution can be predicted. Therefore, in this research, CFD was adopted for numerical simulation analysis, and a neural network was used for the prediction.

In this study, aiming at the problem of pre-dehumidification, a simulation model of an RFC and DV system was established. ANSYS Fluent 16.2 software was used to simulate the thermal and humidity environments of an office located in Jinan, China, in the summer. The determination of how to increase the air supply flow rate (V_{as}) and how to reduce the air supply humidity ratio (H_{as}) and the air supply temperature (T_{as}) was explored, and the effects of the floor temperature (T_{floor}), initial indoor temperature (T_{ini}) and relative humidity (H_{ini}) on the duration and energy consumption of the pre-dehumidification stage were further improved. Then, a back-propagation (BP) neural network prediction model was built in Python, and

the learning sample data set was obtained by simulating the system built in ANSYS Fluent 16.2 software. The data set was then used as the input to learn and train the BP neural network prediction model, and the pre-dehumidification duration and energy consumption were then predicted.

Numerical methods

Description of the simulation model

A typical office located in Jinan, China, was considered the study object of the simulation analysis conducted in this research. The size of the office was 6.0 × 4.5 × 2.5 m, and the heat sources included office workers, computers and a lamp, the heat flux values of which were respectively 147, 370 and 40 W. Fresh air was delivered into the room through two inlets located on the underside of the floor, and the outlet was located near the ceiling. The dimensions of the inlet and outlet were 0.2 × 0.8 m and 0.2 × 0.25 m, respectively. The moisture was considered mainly generated by the adult male occupants at 109 g/h in their sitting positions.[39] The geometric model of the pre-dehumidification stage is illustrated in Figure 1, and the detailed configuration of the simulation model and the heat sources are described in Table 1. Because the phenomenon of dew condensation on the floor is mainly caused by the airflow near the floor, the vertical zone section z = 0.1 m closest to the floor was the main focus of this study.

Table 1. The model parameters and cooling loads.

Item	Dimensions	Cooling load (W)
Human model	0.3×0.4×1.2 (m^3)	147×2
Air inlet	0.2×0.8 (m^2)	N.A.
Computer	0.45×0.45×0.45 (m^3)	370×2
Window	1.2×1.5 (m^2)	N.A.
Lamp	0.15×0.2×1.2 (m^3)	40
Air outlet	0.2×0.25 (m^2)	N.A.
Bookcase	1.05×0.4×1.8 (m^3)	N.A.

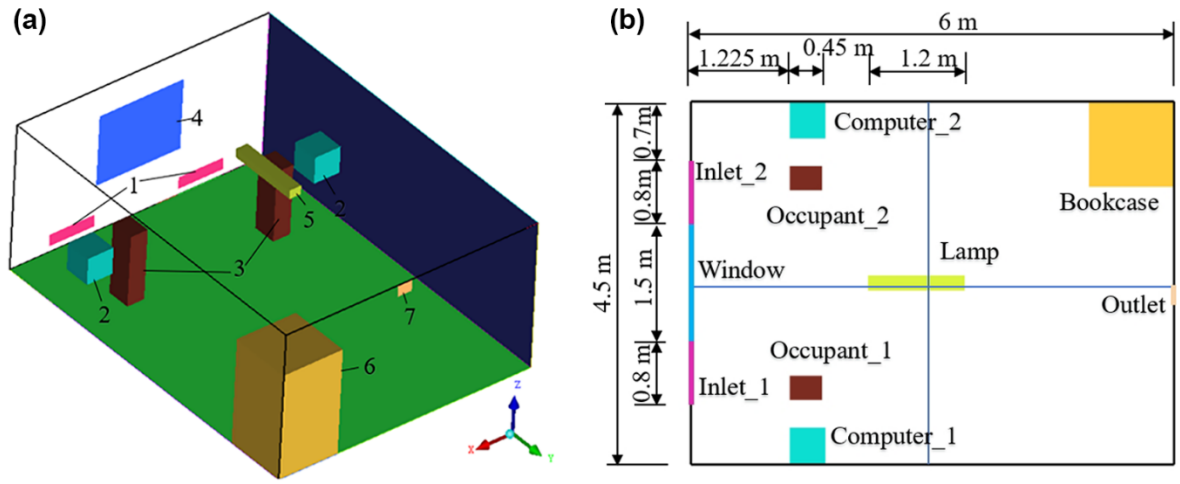

Figure 1. The schematic diagram of the model: (a) the configuration of the simulated office (1-Air inlet; 2-Computer; 3-Human model; 4-Window; 5-Lamp; 6-Bookcase; 7-Air outlet); (b) the arrangement of the equipment in the simulated office.

Mathematical model and numerical schemes

The commercial CFD software ANSYS Fluent 16.2 was used to model the performance of the RFC and DV system. The temperature difference in the considered space was assumed to be low. Therefore, the Boussinesq approximation could be employed to consider the effect of density changes. The flow was assumed to be turbulent, and the air was considered an incompressible gas that includes both dry air and water vapour. Considering the assumptions, the governing equations, including the continuity, momentum and energy equations, are respectively defined as Equations (1) - (3).[40]

$$\frac{\partial \rho}{\partial t} + \frac{\partial (\rho u_j)}{\partial x_j} = 0 \tag{1}$$

$$\frac{\partial (\rho u_i)}{\partial t} + \frac{\partial (\rho u_i u_j)}{\partial x_j} = -\frac{\partial p}{\partial x_i} + \frac{\partial}{\partial x_i}\left((\mu + \mu_i)\frac{\partial u_i}{\partial x_j}\right) + g_i \beta (T - T_0) \tag{2}$$

$$\frac{\partial(\rho c_p T)}{\partial t} + \frac{\partial(\rho c_p T u_j)}{\partial x_j} = \frac{\partial}{\partial x_j}\left((\lambda + \lambda_t)\frac{\partial T}{\partial x_j}\right) \quad (3)$$

where u is the fluid velocity, p is the pressure and T denotes the temperature. Moreover, ρ, μ, c_p and λ are respectively the density, viscosity, heat capacity and conductivity, g is the acceleration term and β denotes the thermal expansion factor.

For the calculation of the thermal comfort and humidity of the air, the species in the transport equation would need to be solved, which are defined by Equation (4).[40]

$$\frac{\partial(\rho Y_i)}{\partial t} + \frac{\partial(\rho u_j Y_i)}{\partial x_j} = \frac{\partial}{\partial x_j}\left((D + D_t\frac{\partial Y_i}{\partial x_j}\right) + S \quad (4)$$

where Y_i is the mass fraction of the species (i), and D is the binary diffusion coefficient. The last term denotes the source term of the species (i).

To better predict the indoor airflow, a suitable turbulence model was selected from various existing models. A study by Chen[41] revealed that the renormalized group (RNG) k-ε turbulence model achieved the best performance among all the eddy-viscosity models for the simulation of mixed convection flow. Therefore, the RNG k-ε turbulence model defined as Equations (5) and (6) was implemented in this study to predict the indoor airflow.[42]

$$\frac{\partial(\rho k)}{\partial t} + \frac{\partial(\rho u_i k)}{\partial x_i} = \frac{\partial}{\partial x_j}\left((\mu + \frac{\mu_t}{\sigma_k})\frac{\partial_k}{\partial x_j}\right) + G - \rho\varepsilon + G_B - \rho D \quad (5)$$

$$\frac{\partial(\rho \varepsilon)}{\partial t} + \frac{\partial(\rho u_i \varepsilon)}{\partial x_i} = \frac{\partial}{\partial x_j}\left((\mu + \frac{\mu_t}{\sigma_k})\frac{\partial_\varepsilon}{\partial x_j}\right) + (C_{1\varepsilon} f_1 G - C_{2\varepsilon} f_2 \rho\varepsilon + C_{3\varepsilon} G_B)\frac{\varepsilon}{k} + \rho E \quad (6)$$

where k and ε are the turbulent kinetic energy and turbulent dissipation rate, respectively. The production of turbulent kinetic energy due to velocity gradients (G) and buoyancy effects (G_B) is respectively defined as Equations (7) and (8).

$$G = \mu_i(\frac{\partial u_i}{\partial x_j} + \frac{\partial u_j}{\partial x_i})\frac{\partial u_i}{\partial x_j} \quad (7)$$

$$G_B = \beta_g \frac{\mu_t}{Pr_t}\frac{\partial T}{\partial x_i} \quad (8)$$

The turbulent viscosity (μ_t) was calculated according to the turbulent kinetic energy (k) and dissipation rate (ε), and is defined by Equation (9).

$$\mu_t = \rho C_\mu f_\mu \frac{k^2}{\varepsilon} \quad (9)$$

The additional terms, which were added due to the Reynolds averaging in the energy and species transport equations, were modelled using the turbulent Prandtl (Pr_t) and Schmidt (Sc_t) numbers, which are respectively defined by Equations (10) and (11).

$$Pr_t = \frac{v_t}{\alpha_t} = \frac{\mu_t}{\lambda_t / C_p} \quad (10)$$

$$Sc_t = \frac{v_t}{D_t} \quad (11)$$

To achieve the phenomenon of water vapour being generated from the human body and diffusing into the surrounding environment, the human body was set as a zone to release heat and water vapour. The surrounding air was heated through the surface of the human body, and other heat sources released heat from the surface at a constant heat flow rate.

Standard wall treatment was chosen to treat the near-wall airflow. The semi-implicit method for pressure-linked equations (SIMPLE) algorithm was chosen for pressure and velocity field coupling, and the second-order upwind discretization scheme was chosen to solve all the variables in the simulation cases, excluding the pressure, which was solved by a staggered scheme called pressure staggering option (PRESTO!). The Green-Gauss cell-based method was used for the gradient. Considering that the model contained a large number of complex geometric surfaces and the influence of thermal buoyant force, the discrete ordinate (DO) radiation model was used to simulate the transfer of radiation heat emitted from the internal objects. The details of the numerical methods and boundary conditions are summarized in Table 2.

Table 2. The details of the numerical methods and simulation setup.

Turbulence model	RNG k-ε turbulence model
Species model	Species transport
Numerical schemes	For pressure, the staggered third scheme PRESTO!; for other terms, the second-order upwind discretization scheme and the SIMPLE algorithm

Boundary condition setup

The rate of floor temperature cooling was slow when the RFC system was operated, and due to the moisture of the human body, the air dew point temperature (T_{ad}) near the floor would gradually increase and

soon become higher than T_{floor}, which would cause condensation. Therefore, the DV system would need to operate in advance for pre-dehumidification, and the key is the difference between T_{floor} and T_{ad}. In the simulation, the RFC system was open when T_{ad} was lower than T_{floor} = 2°C. The air inlet was set as the velocity inlet boundary condition, and the air outlet was set as the pressure outlet boundary condition. Because more than one factor could affect T_{ad}, three air supply factors that could affect the duration and energy consumption of pre-dehumidification were considered, namely T_{as}, H_{as} and V_{as}. The values of V_{as} were selected as 0.016, 0.024 and 0.036 m^3/s, which were designed to satisfy the outdoor ventilation rate recommended in a previous study.[43] Moreover, according to another study, the air supply temperature was at least 2°C lower than the indoor air temperature;[44] thus, the values of T_{as} were selected as 21, 22 and 23°C, and the values of H_{as} were selected as 10, 10.5 and 11 g/kg.

According to previous research,[45,46] the air supply was efficiently spread along the floor at temperatures T_{floor} below 25°C, and T_{floor} should not be lower than 18°C when the RFC system was adopted. Therefore, the floor was set as a constant-temperature surface, and the values of T_{floor} in the simulation were selected as 22, 23 and 24°C. In addition, T_{ini} and H_{ini} were also considered, and the values of T_{ini} were selected as between 26 and 28°C based on the floor surface temperature. The selection range of H_{ini} was from 14.7 to 18.88 g/kg, as shown in Figure 2. In the figure, zones "a" and "b" indicate the selection ranges of T_{ini} and H_{ini} when T_{floor} = 22°C, and T_{ad} ranged from 20 to 22°C; zones "b" and "c" indicate the selection ranges of T_{ini} and H_{ini} when T_{floor} = 23°C, and T_{ad} ranged from 21 to 23°C; zones "c" and "d" indicate the selection ranges of T_{ini} and H_{ini} when T_{floor} = 24°C, and T_{ad} ranged from 22 to 24°C. Based on this, the selected values of different influencing factors are exhibited in Table 3, and the selection of the simulation parameters generated 243 data sets under different combinations of the five variables. The personnel and equipment cooling were ignored, as there was no occupant in the numerical simulation of pre-dehumidification. Considering the building that housed the office, and considering that work commences at 08:00, negligible solar radiation and negligible infiltration of doors and windows were assumed in the pre-dehumidification stage. The ceiling, side walls and the window were set as constant-temperature surfaces, and the bookcase was set as the adiabatic boundary condition. Moreover, the outdoor temperature was assumed 30°C and the relative humidity was 80%. Table 4 shows the detailed boundary conditions established in the CFD simulation.

Table 3. The parameter setup for different simulation cases.

Parameters	Selected values	Unit
V_{as}	0.016, 0.024, 0.032	m^3/s
T_{as}	21, 22, 23	°C
H_{as}	10, 10.5, 11	g/kg
T_{floor}	22, 23, 24	°C
T_{ini} and H_{ini}	Case 1* (26.5,76.12), (27,78.57), (28,78.71) Case 2** (26,76.04), (26.5,78.5), (27.5,78.64) Case 3*** (26,73.71), (26.5,76.12), (27.5,76.27)	°C, %

*: the selected values of T_{ini} and H_{ini} when T_{floor} = 22°C
**: the selected values of T_{ini} and H_{ini} when T_{floor} = 23°C
***: the selected values of T_{ini} and H_{ini} when T_{floor} = 24°C

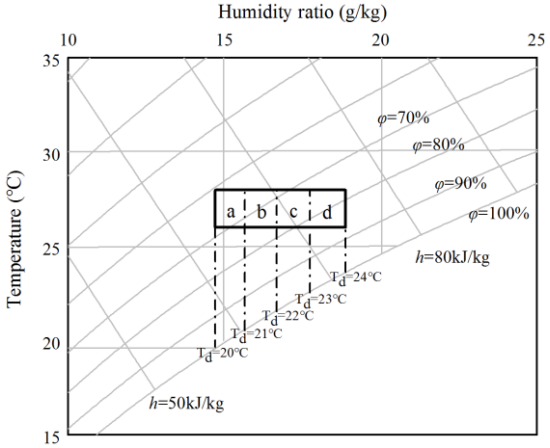

Figure 2. The initial conditions located in the i-d diagram, including zones "a," "b," "c" and "d".

Table 4. The boundary condition setup in the CFD simulation.

Boundary	Simulation setup
Air inlet	Velocity inlet
Air outlet	Pressure outlet
Ceiling	Constant temperature, 26°C
Walls	Constant temperature, 26°C
Window	Constant temperature, 26°C
Floor	Constant temperature, 20, 21 and 22°C
Occupants	Uniform heat flux, 147 W
Lamp	Uniform heat flux, 40 W
Computer	Uniform heat flux, 370 W
Bookcase	Adiabatic wall
Outdoor weather	Temperature, 30°C; relative humidity, 80%

Energy demand for ventilation

CFD simulation has been widely used for the prediction of airflow in office environments. However, issues regarding heat transfer and energy usage in office spaces have not been successfully addressed using CFD techniques. The primary interest of this study is the pre-dehumidification stage, in which only the DV system was operated. Based on a survey of previous experimental and numerical research on the quantification of the energy efficiency of ventilation systems, the energy used by the ventilation system was divided into two main components,[47] namely the fan and cooling energy consumption, both of which could be derived from the CFD estimations.

(1) Fan energy consumption

Fan energy is an important factor in annual energy consumption and is defined by Equation (12).[48]

$$E_{fan} = \frac{p_{vent}}{3600 \times \eta_1 \times \eta_2} V_{as} \tau_{pre} \quad (12)$$

where E_{fan} is the fan energy consumption (kWh), p_{vent} is the full pressure of the fresh air unit (Pa), V_{as} is the air supply flow rate (m^3/h), τ_{pre} is the pre-dehumidification duration (h), η_1 is the transmission efficiency, the value of which was considered 0.85, and η_2 is the fan efficiency, the value of which was considered 0.78.

(2) Cooling energy consumption

In light of the previous methods used for energy usage prediction with alternate ventilation systems, the cooling energy requirement can be subdivided into two portions. This study mainly analyzed the pre-dehumidification stage, in which only the DV system was operated. Therefore, the energy consumption generated by cooling coils to eliminate the heat load of the indoor space was not included in the calculation of cooling energy consumption. Only the cooling energy portion used to condition the outdoor fresh air to the air supply state was included. According to the calculation of cooling energy consumption in previous studies,[49,50] the calculation of this portion of energy consumption was according to Equation (13).[50]

$$E_{vent} = V_{as} \rho (h_{out} - h_{as}) \tau_{pre} \quad (13)$$

where E_{vent} is the portion of cooling energy used to condition the outdoor fresh air to the air supply state (kWh), ρ is the air density, the value of which was assumed to be 1.29 kg/m^3, and h_{out} and h_{as} are respectively the specific enthalpies of the outdoor and supply air (kJ/kg).

As a supplement to the previous statement, the following assumptions were imposed on the energy analysis for the ventilation system. The energy used by the condenser water pump, chilled water pump and fans in the cooling tower was excluded. The chilled water heat exchanger was presumed to work under perfect conditions, i.e., the heat transfer efficiency in each component was assumed to be 1. The ducts were assumed to be perfectly tight, and airflow through the ductwork was adiabatic. There was no temperature gradient along the duct when there was no other energy generation equipment. Finally, the effect of the fan power on the supply air temperature was neglected.[50]

Grid independence analysis

ANSYS ICEM CFD software was used to generate structured hexahedral meshes for the studied model. Due to the large variations of the temperature and velocity gradients around the heat sources (the human body and equipment), the resulting grid was fine enough to capture the thermal environment behaviour and solve the boundary layer. In other regions where the temperature and velocity gradients changed little and the flow characteristics were relatively consistent, the grid was relatively sparse. Grid independence tests play an important role in the accuracy of the results and the prediction cost of CFD simulation. Therefore, coarse, medium and fine grids were selected to study the grid independence of the numerical simulation conducted in this study. The case with specific values of T_{as}, H_{as}, V_{as}, T_{floor} and T_{ini} and H_{ini} was taken as an example to evaluate the performance of different numbers of grids, as listed in Table 5. The values of T_{as}, H_{as}, V_{as}, T_{floor} and T_{ini} and H_{ini} were selected as 23°C, 11 g/kg, 0.032 m^3/s, 22°C and 28°C and 78.71%, respectively. The temperature and humidity results of section z = 0.1 m were compared. Figure 3 presents

the variations of the temperature and humidity under different grids. By comparing the simulation results, there were no significant variations in temperature and humidity distributions with the increase of the number of grid cells from the medium grid to the fine grid, and the maximum errors of temperature and humidity were 0.058 (0.23%) and 0.093 (0.63%), respectively. Nevertheless, with the increase of the number of grid cells from the coarse grid to the medium grid, the maximum absolute errors of temperature and humidity were 0.08°C and 0.20 g/kg, respectively. Therefore, the medium grid with 529276 computing units was selected for subsequent numerical simulation. The grid diagram is exhibited in Figure 4.

Table 5. The grid independence test.

Item	Total number of elements	Temperature maximum error (°C)	Humidity maximum error (g/kg)
Coarse grid	337542		
Medium grid	529276	0.08	0.20
Fine grid	836336	0.06	0.09

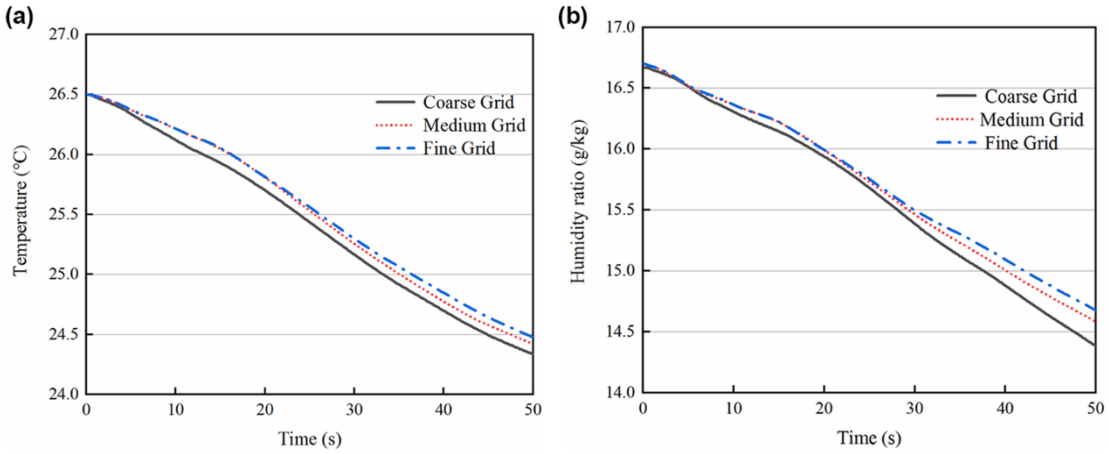

Figure 3. The variations of the (a) temperature and (b) humidity under different grids at z = 0.1 m.

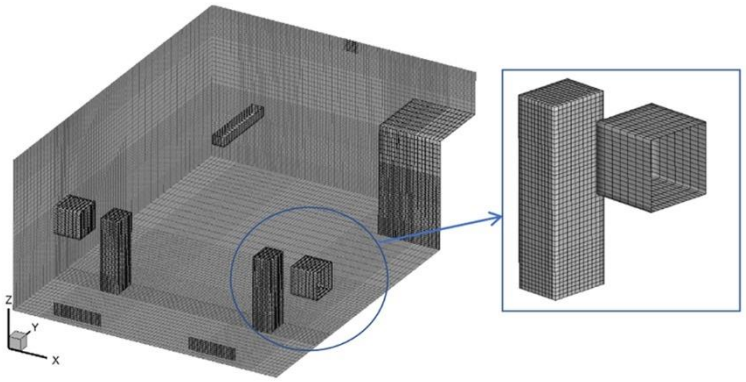

Figure 4. The grid distribution diagram of the medium grid.

Validation of the fluid flow

To verify the accuracy of the RNG k-ε turbulence model in the prediction of the indoor thermal environment, the simulation data of the indoor air velocity and temperature distributions were compared with data from an experimental study by Xu et al.[51]. Figure 5(a) illustrates the schematic diagram of the experimental chamber. The simulation was performed in a typical small room with dimensions of 6.0 × 3.9 × 2.35 m (length × width × height) with two heat sources, including one occupant (76 W) seated in front of a table and one computer (40 W) located on the table. The dimensions of the supply and exhaust diffusers were respectively 0.4 × 0.15 m and 0.34 × 0.14 m. The air supply flow rate was 43 m^3/h, which was equal to 0.79 ACH (air change per hour), and the air supply temperature was 19°C. Different temperature values were used for the bounded walls, ceiling and floor. Two poles, namely poles 1 and 2, were used in this validation to predict the temperature and velocity distributions. The distribution diagrams of the two poles are exhibited in Figure 5(b). Figures 5(c) and 5(d) respectively present the comparisons between the temperature and velocity along the height direction of poles 1 and 2 in the simulation and experiment. Pole 1 exhibited a small temperature difference in the room area of less than 0.5 m. In this area, the simulated temperature was higher than the experimentally measured value. This was because the heat flux of the human

model was constant in the simulation. In contrast, the evenly distribution of the heat flux was difficult in the experiment. The leg area of the mannequin would have a lower heat flux than the rest of the body, and pole 1 was located between the legs; thus, the simulation of pole 1 reflected a higher temperature.

Validation of the humidity distribution

To verify the accuracy of the humidity distribution, the simulation data were compared with data from an experimental study of the indoor humidity distribution conducted by Ma et al.[52] As shown in Figure 6(a), the dimensions of the laboratory were 4 × 3 × 2.5 m (length × width × height). Air entered from the top of one sidewall and was discharged from the bottom of the other sidewall. The indoor ventilation volume was 302 m^3/h, and there was no heat source in the room. The humidification rate was 0.052 g/s. The temperature of all walls was maintained at 22 ± 0.9°C. Points 1 and 2 were used to predict the indoor humidity distribution in the validation study. The location distribution diagrams of the two points are presented in Figure 6(b). Moreover, Figures 6(c) and 6(d) respectively present the comparisons of the humidity ratios obtained from the experimental measurement and the simulation. The simulated data were consistent with most of the experimental measurement data. Point 1 exhibited a deviation in the initial stage, and Ma et al. [52] mentioned that the fluctuation of the experimental measurement data was caused by the instability of the system in the initial stage. Point 1 was close to the entrance; thus, the error between the experimental and simulation data would have been relatively large. The simulation of point 2 was significantly consistent with the experimental data. The good consistency indicates that the accuracy of this model was sufficient for further study.

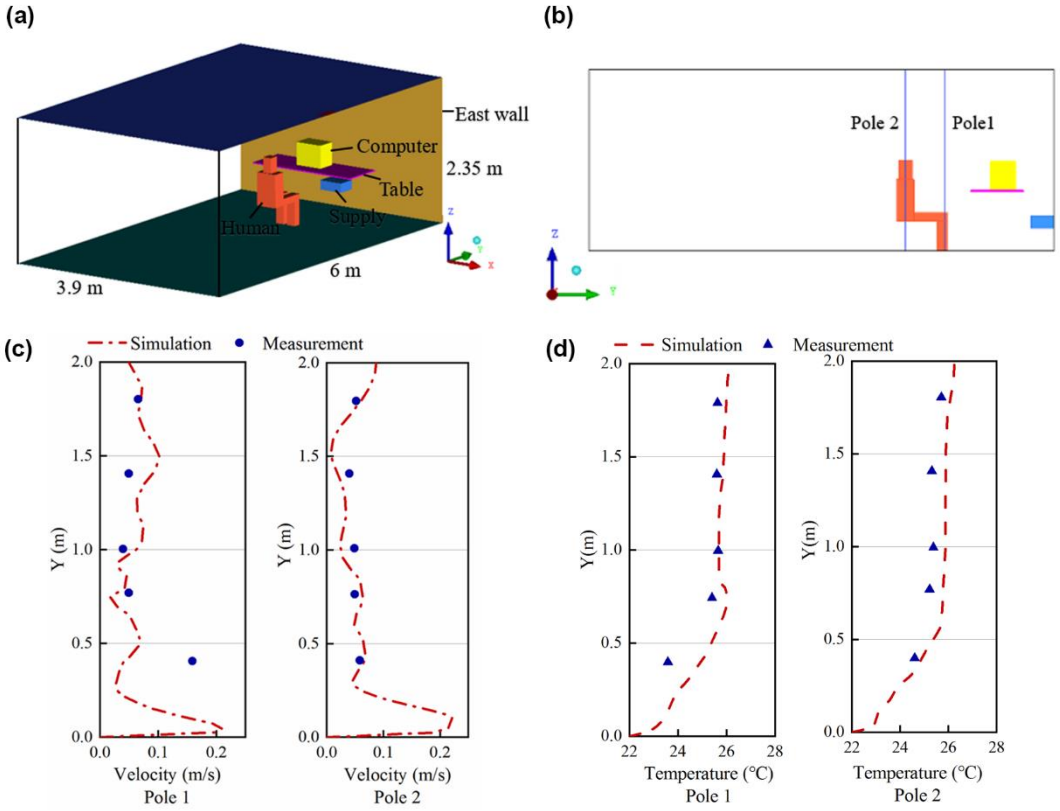

Figure 5. (a) The schematic diagram of the validation room model; (b) the locations of poles 1 and 2; the comparison between the simulated and experimental (c) velocity and (d) temperature at the two poles.

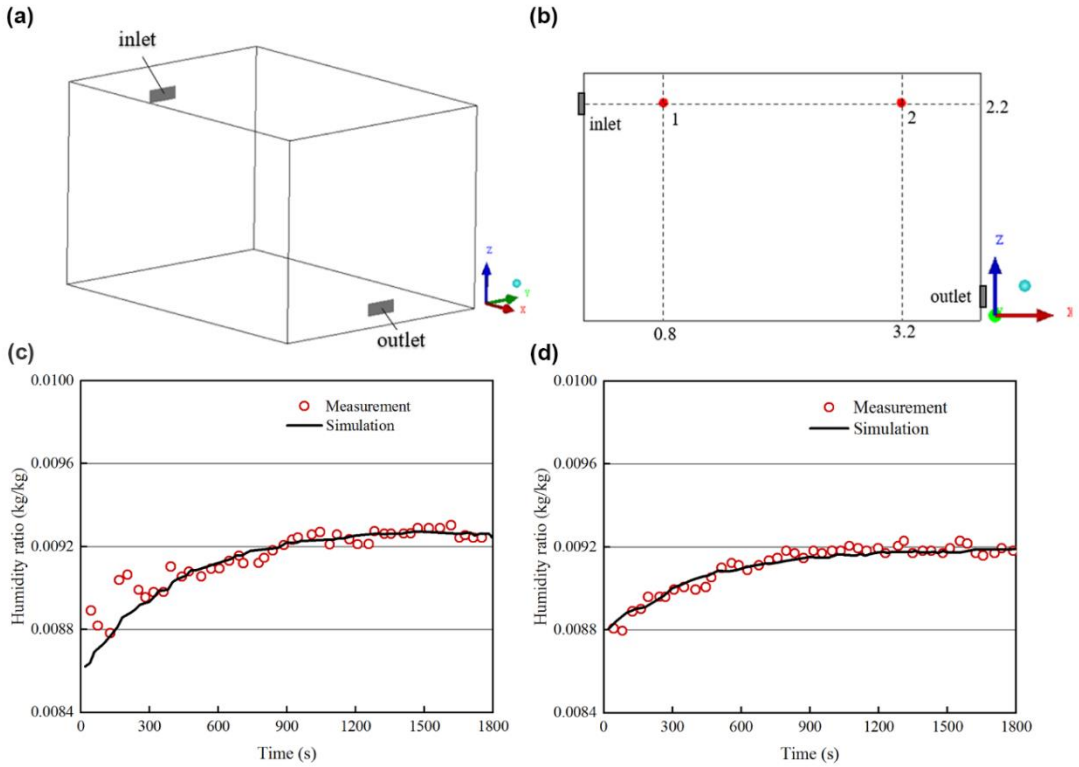

Figure 6. (a) The schematic diagram of the validation room model; (b) the locations of points 1 and 2; the comparison between the simulated and experimental humidity ratios at (c) point 1 and (d) point 2.

BP neural network

An artificial neural network (ANN) is a machine learning tool that can be used to learn the relationships between input and output variables to predict system performance. It works like a black-box model that requires no detailed system parameters.[53] The ANN architecture consists of an input layer, an output layer and one or more hidden layers. Each layer is composed of neurons that receive signals from previous layers and produce outputs based on activation functions.

The most widely used ANN structure in prediction models is the multilayer perceptron (MLP) model. A MLP model with a single hidden layer containing a sufficient number of neurons has been proven[54,55] that it can approximate any function with the desired accuracy. Therefore, a MLP network was established in this study to predict the duration and energy consumption of the pre-dehumidification stage, as shown in Figure 7. The MLP network consists of an input layer, a hidden layer and an output layer, in which all inputs are connected to neurons and all neurons are connected to outputs.

The correlation between the input $u(k)$ and output $y(k)$ in the MLP network can be written mathematically as Equations (14) and (15).[56]

$$y(k) = f_2(w^2 x(k) + b_2) \quad (14)$$

$$x(k) = f_1(w^1 x(k) + b_1) \quad (15)$$

where $x(k)$ indicates the output vector from the hidden layer, and w^2 and w^1 respectively represent the connection weight matrixes from the hidden layer to the output layer and from the input layer to the hidden layer. Moreover, b_1 and b_2 represent bias numbers in the input and output layers, respectively, and $f_1(.)$ and $f_2(.)$ respectively represent the transfer functions of the hidden and output layers. The transfer function used in the present study was a tangent sigmoid function, which can be expressed as Equation (16).[57]

$$f(z) = \frac{(1-e^{-2z})}{(1+e^{-2z})} \quad (16)$$

where z represents a function of $z = f(\sum w_i x_i)$, where i is the index of inputs to the neuron, x_i is the input to the neuron, w_i is the weighted factor attached to the input and z is the weighted input. The prediction accuracy was measured using the root mean square error (RMSE), as defined by Equation (17).[53]

$$RMSE = \sqrt{\frac{1}{p}\sum_j | t_j - o_j |^2} \quad (17)$$

where p represents the number of data sets, t_j is a target and o_j is an output value.

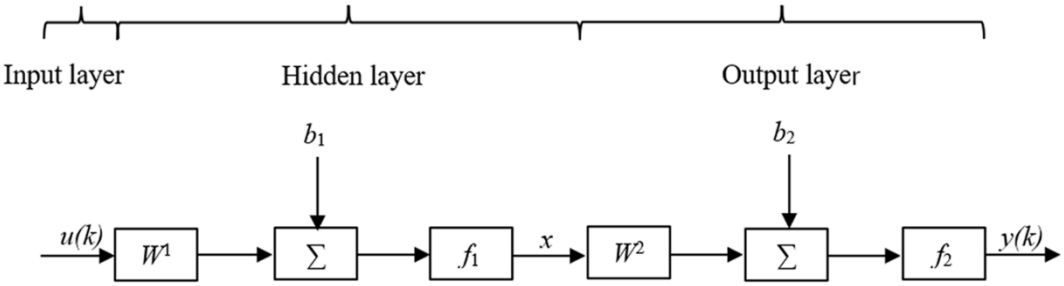

Figure 7. The multilayer perceptron network.

The structure of the ANN is exhibited in Figure 8, and was designed with 5 inputs, 10 neurons and 2 outputs. The inputs were the air supply temperature, air supply humidity ratio, air supply flow rate, floor temperature and initial indoor temperature and relative humidity, respectively. The outputs were the pre-dehumidification duration and energy consumption, respectively. The simulation duration was at least about 4 h and at most nearly 12 h. Nearly 30 days was needed to finish all the simulations. The 243 simulated data were divided into two parts; 80% of the data were randomly selected for neural network training and the remaining 20% were used for validation.

The training process was carried out by optimizing the weights and deviation coefficients to minimize the error between the target and the output of the ANN. The BP neural network was adopted for use in this study. The BP neural network was a multilayer feedforward neural network. Its name was derived from the adjustment rules of network weights, for which the error back-propagation learning algorithm was used. The sample was submitted to the network, and the size of the error was preset according to the training of the error limit. When the network converges, the training ends. When the number of training iterations has reached the maximum, the training was terminated, and when the network cannot converge, this represents the end of the learning process. The error propagation process was then reversed, and training was carried out continuously according to the error feedback until the condition was satisfied or until the network was trained to the maximum number of iterations.[58]

The BP neural network is mainly used in function approximation, relation identification, data classification and data compression. The use of the BP neural network as the core of the prediction model can theoretically yield the approximation of any nonlinear model by taking advantage of its function approximation feature. Figure 9 presents the flowchart of the BP neural network algorithm. The learning process of the BP neural network was divided into a forward calculation process, reverse calculation process and memory training process. During the forward calculation process, the input signal was received by the input layer, processed by the hidden layer and then transmitted to the output layer. After the forward calculation process, if the output obtained by the output layer was not the desired output, the reverse propagation stage of the error was entered, i.e., the output error signal returned along the connection path of the neurons, from the output layer to the hidden layer and then back to the input layer. The weight of the neuron in each layer was modified according to the received error signal to minimize the error signal. During the memory training process, the weights of neurons were constantly adjusted. To obtain the preset error value, the forward calculation and reverse calculation of the BP neural network were carried out alternately until the error reached the allowable range, or until the maximum number of iterations of the algorithm was reached.

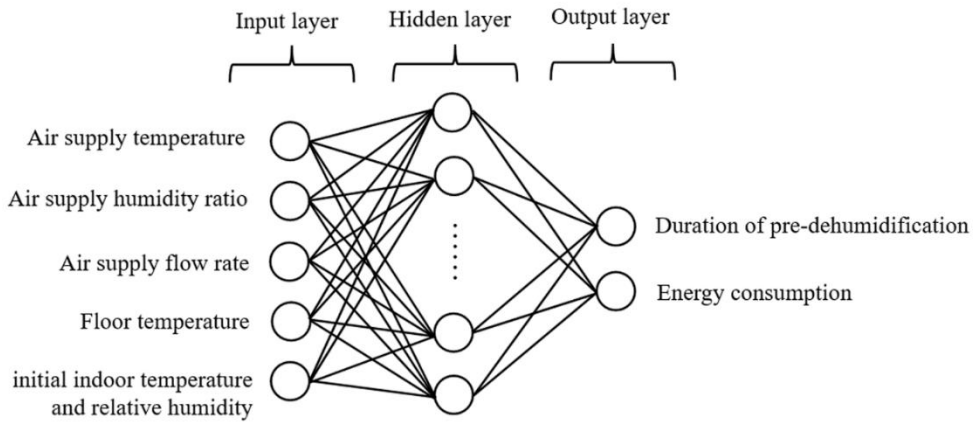

Figure 8. The structure of the neural network with inputs and outputs.

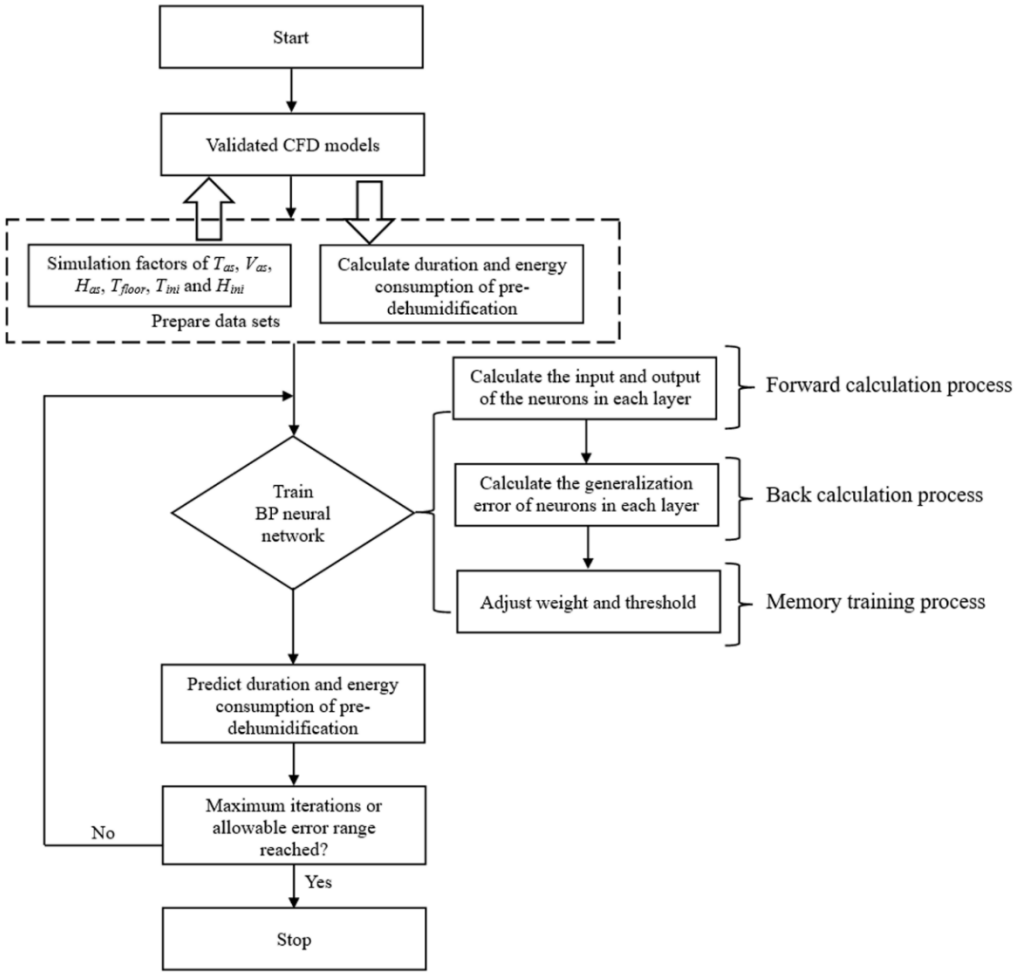

Figure 9. The flow chart of the BP neural network algorithm.

Results and discussion

Analysis results of CFD simulation

Distributions of the indoor air temperature and humidity

According to the calculation of simulation results, when T_{as}, V_{as}, H_{as}, T_{floor} and T_{ini} and H_{ini} were 23°C, 0.016 m^3/s, 11 g/kg, 22°C and 26.5°C and 76.12%, respectively, the pre-dehumidification duration was 120 s. Due to the long pre-dehumidification duration and the temperature and humidity variations, this simulated case was further investigated. To better understand the variations in the indoor temperature and humidity in

the pre-dehumidification stage, another case of V_{as} = 0.024 m^3/s with other factors remaining unchanged was selected for further investigation. The section y = 1.425 m was used to study the temperature and humidity environment, as shown in Figure 10.

Figures 11 and 12 respectively present the air temperature and humidity contours at y = 1.425 m at different times when V_{as} = 0.016 m^3/s. The distributions of the indoor temperature and humidity exhibited stratification phenomena. The temperature and humidity gradually increased from bottom to top. Due to the low temperature and humidity of the air entering the room from the inlet near the ground, the temperature and humidity at the bottom of the room were usually relatively low. As the ventilation time was increased, the low temperature and humidity of the air near the floor were both gradually increased. Figure 11(a) exhibits the air temperature contour at τ = 40 s, the 299.6 K contour line was shown 0.22 m away from the ground. As shown in Figure 11(c), the ventilation time was increased to 120 s till the end of pre-dehumidification, the contour line rose to close to 0.35 m. In addition, with the increase in the ventilation time, the bottom 295.6 K contour line also gradually rose from 0 m to about 0.35 m above the ground. Regarding the humidity, the same effect as presented in Figure 11 is exhibited in Figure 12. Taking the 0.0165 contour line as an example, with the increase in the ventilation temperature, the area of low-humidity air at the bottom was increased gradually; moreover, the 0.0165 contour line was 0.15 m from the ground after 40 s, and 0.27 m from the ground after 120 s.

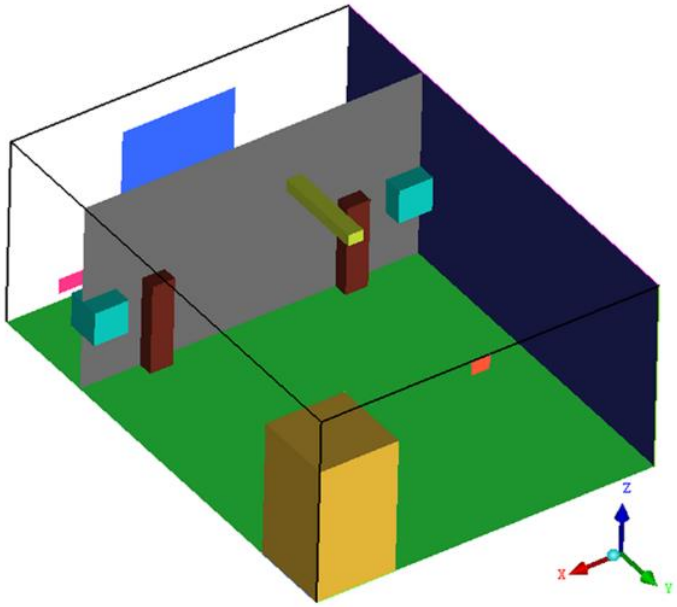

Figure 10. The schematic diagram of the study section y = 1.425 m.

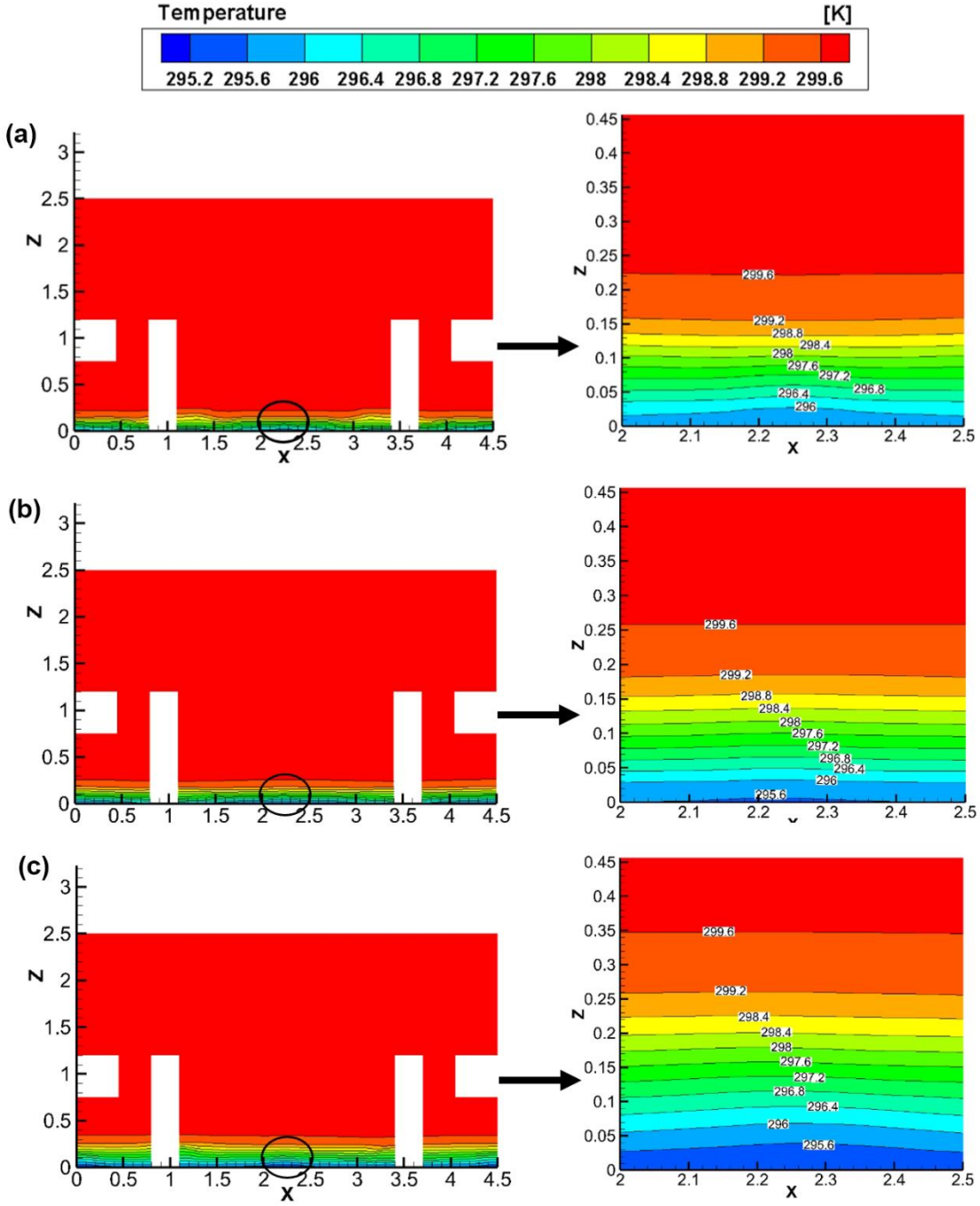

Figure 11. The air temperature contours at y = 1.425 m when V_{as} = 0.016 m^3/s: (a) the air temperature at τ = 40 s; (b) the air temperature at τ = 80 s; (c) the air temperature at τ = 120 s.

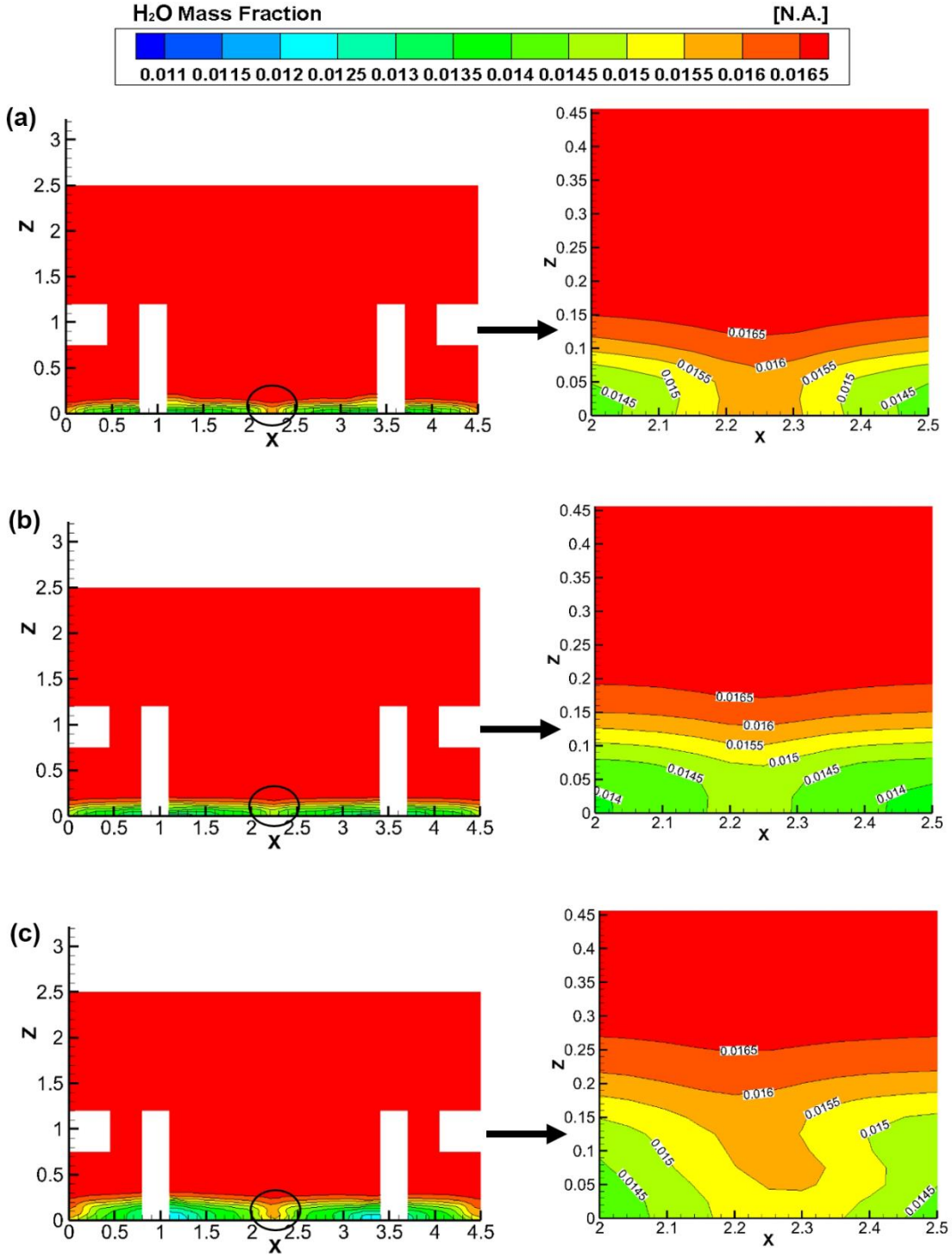

Figure 12. The air humidity contours at y = 1.425 m when V_{as} = 0.016 m^3/s: (a) the mass fraction of H_2O at τ = 40 s; (b) the mass fraction of H_2O at τ = 80 s; (c) the mass fraction of H_2O at τ = 120 s.

Figures 13 and 14 respectively present the air temperature and humidity contours at y = 1.425 m at different times when V_{as} = 0.024 m^3/s. Figure 13(a) presents the air temperature contour at τ = 35 s; taking the 299.6 K contour line as an example, the contour line was 0.225 m away from the ground at τ = 35 s, which could achieve the effect of V_{as} = 0.016 m^3/s and τ = 40 s. Figure 13(b) presents the air temperature contour at τ = 70 s; the 299.6 K contour line was 0.25 m away from the ground, which could achieve the effect of V_{as} = 0.016 m^3/s and τ = 80 s. Figure 14 presents the air humidity contour; taking the 0.0165 contour line as an example, the contour line was 0.16 m away from the ground at τ = 35 s and 0.195 m away from the ground at τ = 75 s, which could achieve the effects of V_{as} = 0.016 m^3/s and the ventilation times of 40 and 80 s, respectively. These phenomena all demonstrate that increasing the value of V_{as} can effectively

shorten the pre-dehumidification duration and increase the area at the bottom representing low-temperature and low-humidity air. Furthermore, the pre-dehumidification stage had been completed when V_{as} = 0.024 m^3/s with τ = 70 s.

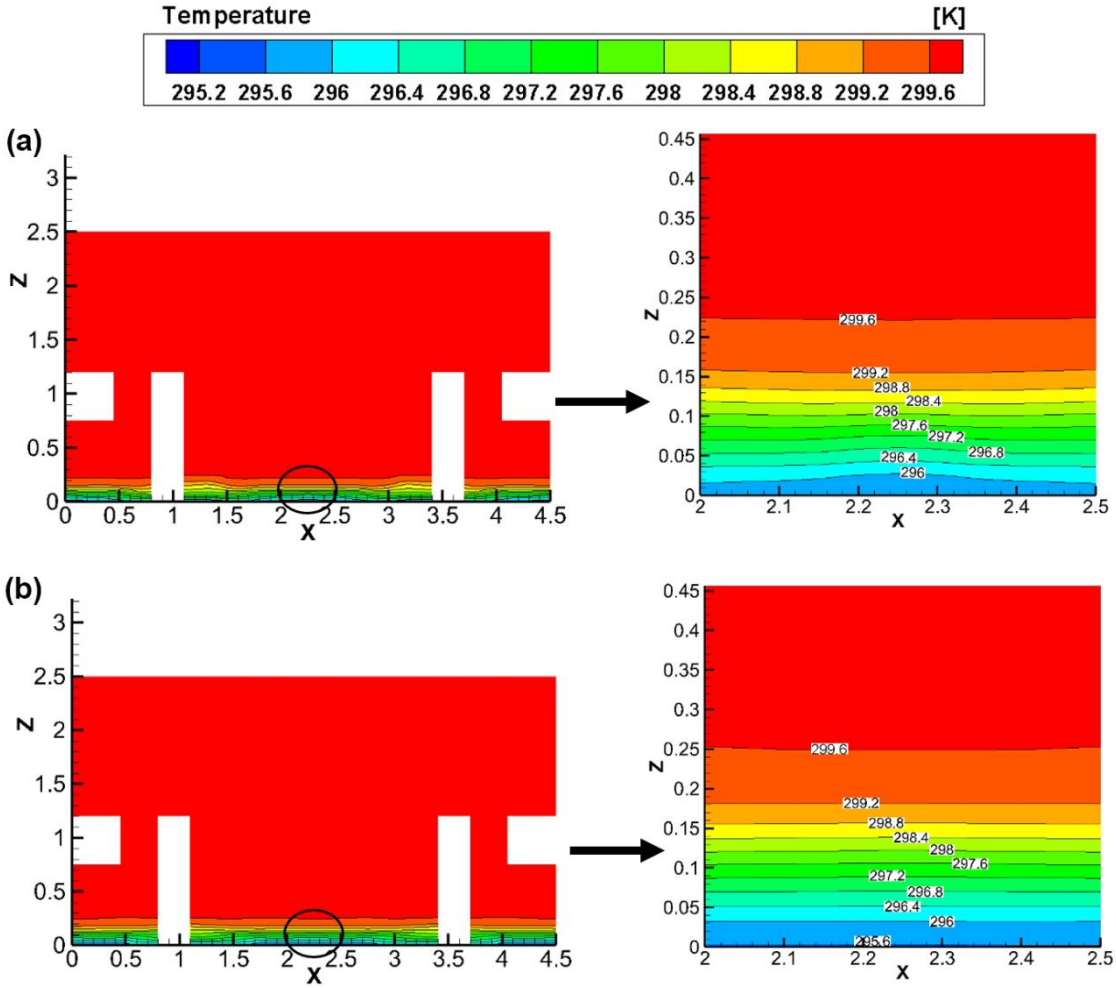

Figure 13. The air temperature contours at y = 1.425 m when V_{as} = 0.024 m^3/s: (a) the air temperature at τ = 35 s; (b) the air temperature at τ = 70 s.

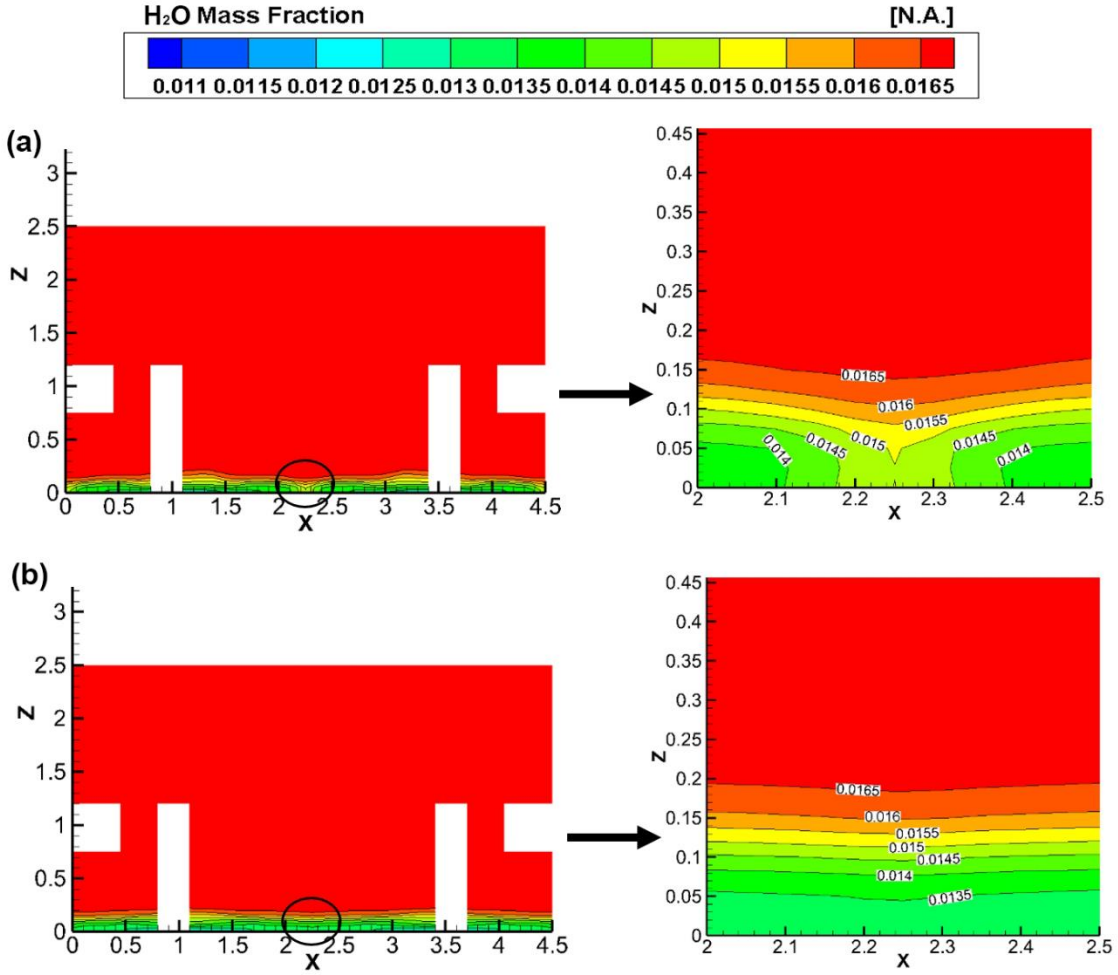

Figure 14. The air humidity contours at y = 1.425 m when V_{as} = 0.024 m^3/s: (a) the mass fraction of H_2O at τ = 35 s; (b) the mass fraction of H_2O at τ = 70 s.

Simulation results of the effects of the control factors

Eleven cases were selected for the comparative analysis of the effects of T_{as}, V_{as}, H_{as}, T_{floor} and T_{ini} and H_{ini} on the pre-dehumidification duration and energy consumption. For the energy consumption, an office building was taken as an example for the analysis. The building was assumed to be 5 floors, and each floor had 20 rooms. The analyses of the pre-dehumidification duration and energy consumption are provided as follows.

Figure 15(a) exhibits the effects of the variation in T_{as} on the pre-dehumidification duration and energy consumption. Regarding the pre-dehumidification duration, when T_{as} = 23, 22 and 21°C, the pre-dehumidification duration was respectively 45.5, 45.3 and 45.2 s, and the maximum time difference was only 0.3 s. With the decrease in T_{as} from 23 to 21°C, the pre-dehumidification stage was only shortened by 0.65%. Thus, reducing T_{as} was found to have no significant effect on the pre-dehumidification duration. Regarding the energy consumption, when T_{as} = 23, 22 and 21°C, the energy consumption was respectively 2.27, 2.31 and 2.36 kWh. With the decrease in T_{as} from 23 to 21°C, the energy consumption was increased by 3.8%. According to Equations (12) and (13), with the variation of T_{as}, the energy consumption was related to the pre-dehumidification duration and the difference in the enthalpy of the air supply and the outdoor air. The effect of T_{as} on the pre-dehumidification duration was found to be very small. Thus, the energy consumption mainly depended on the difference in the enthalpy of the air supply and the outdoor air. The greater the value of T_{as}, the smaller the difference in the enthalpy of the air supply and outdoor air. Hence, if T_{as} increases, the energy consumption will decrease.

Figure 15(b) exhibits the effects of the variation of H_{as} on the pre-dehumidification duration and energy consumption. Regarding the pre-dehumidification duration, when H_{as} = 10, 10.5 and 11 g/kg, the pre-dehumidification duration was respectively 39.7, 42.2 and 45.5 s. With the decrease in H_{as} from 11 to 10 g/kg, the pre-dehumidification duration was shortened by 12.7%. Regarding the energy consumption, when H_{as} = 10, 10.5 and 11 g/kg, the energy consumption was respectively 2.10, 2.21 and 2.27 kWh. With the

decrease of H_{as} from 11 to 10 g/kg, the energy consumption was reduced by 7.5%.

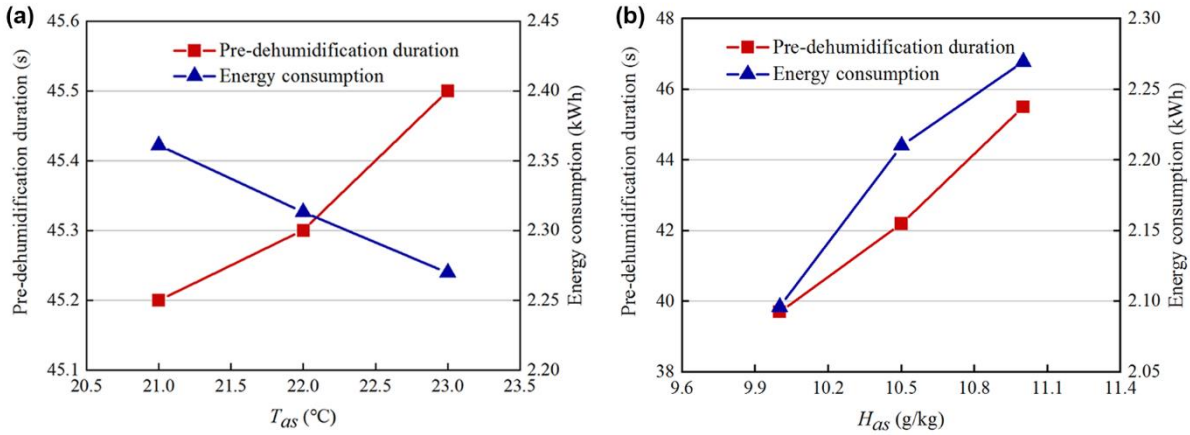

Figure 15. The effects of the variations in (a) T_{as} and (b) H_{as}.

Figure 16(a) presents the effects of the variation in V_{as} on the pre-dehumidification duration and energy consumption. Regarding the pre-dehumidification duration, when V_{as} = 0.016, 0.024 and 0.032 m^3/s, the pre-dehumidification duration was respectively 45.4, 60.2 and 96.7 s. With the increase in V_{as} from 0.016 to 0.032 m^3/s, the pre-dehumidification duration was shortened by 52.7%. According to the comparative analysis data, the increase in V_{as} had the most significant effect on the pre-dehumidification duration. Regarding the energy consumption, when V_{as} = 0.016, 0.024 and 0.032 m^3/s, the energy consumption was respectively 2.41, 2.25 and 2.27 kWh. With the increase in V_{as} from 0.016 to 0.024 m^3/s, the energy consumption was decreased by 6.6%. With the increase in V_{as} from 0.024 to 0.032 m^3/s, the energy consumption was increased by 0.8%.

Figure 16(b) presents the effects of the variation in T_{floor} on the pre-dehumidification duration and energy consumption. Regarding the pre-dehumidification duration, when T_{floor} = 22, 23 and 24°C, the pre-dehumidification duration was respectively 51.4, 45.5 and 41.1 s. With the increase in T_{floor} from 22 to 24°C, the pre-dehumidification duration was shortened by 20%. Regarding the energy consumption, when T_{floor} = 22, 23 and 24°C, the energy consumption was respectively 2.56, 2.27 and 2.05 kWh. With the increase in T_{floor} from 22 to 24°C, the energy consumption was decreased by 19.9%.

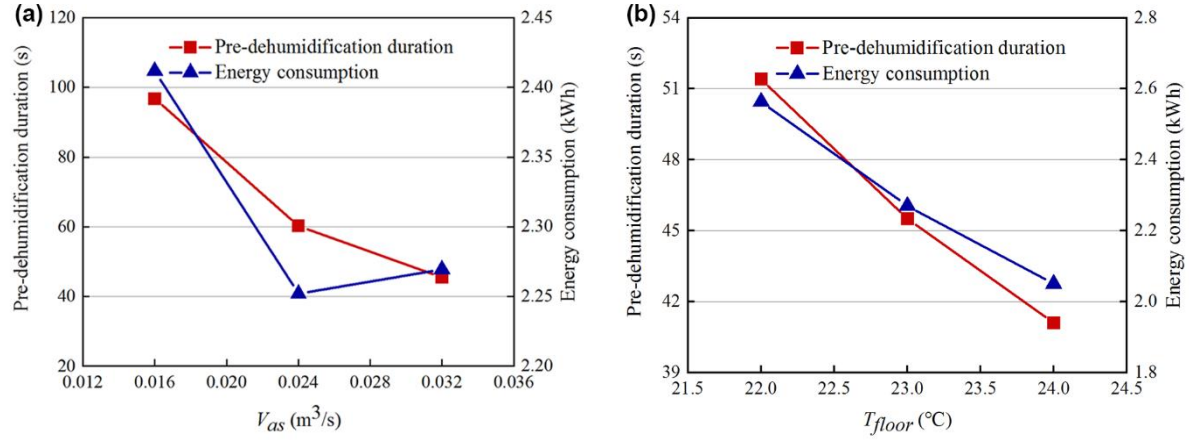

Figure 16. The effects of the variations in (a) V_{as} and (b) T_{floor}.

Figure 17 exhibits the effects of the variation of T_{ad} on the pre-dehumidification duration and energy consumption. Because T_{ini} and H_{ini} are directly related to T_{ad}, T_{ad} was used to represent the effects of T_{ini} and H_{ini} on the pre-dehumidification duration and energy consumption. Regarding the pre-dehumidification duration, when T_{ad} = 22, 22.5 and 23°C, the pre-dehumidification duration was respectively 31, 39.1 and 45.5 s. With the decrease in the initial indoor T_{ad} from 23 to 22°C, the pre-dehumidification duration was shortened by 31.8%. Regarding the energy consumption, when the initial indoor T_{ad} = 22, 22.5 and 23°C, the energy consumption was respectively 1.54, 1.95 and 2.27 kWh. With the decrease in the initial indoor T_{ad} from 23 to 22°C, the energy consumption was decreased by 32%.

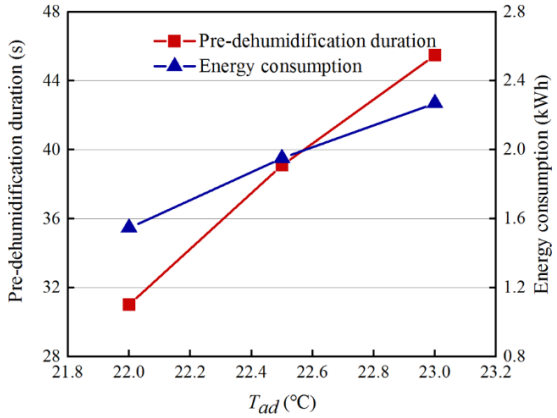

Figure 17. The effects of the variation in T_{ad}.

Training and validation results of the BP neural network model

Training results for the duration and energy consumption of pre-dehumidification

Figures 18 and 19 exhibit the training results of the BP neural network for the duration and energy consumption of pre-dehumidification. The values obtained by the BP neural network almost coincided with the CFD simulation values. The coefficient of determination (R^2) and RMSE values of the training results for the pre-dehumidification duration were respectively 0.9962 and 1.2267, and the values of the pre-dehumidification energy consumption were respectively 0.9897 and 0.0004. The R^2 values of both the duration and energy consumption of pre-dehumidification were high, indicating that the training results of the BP neural network were better.

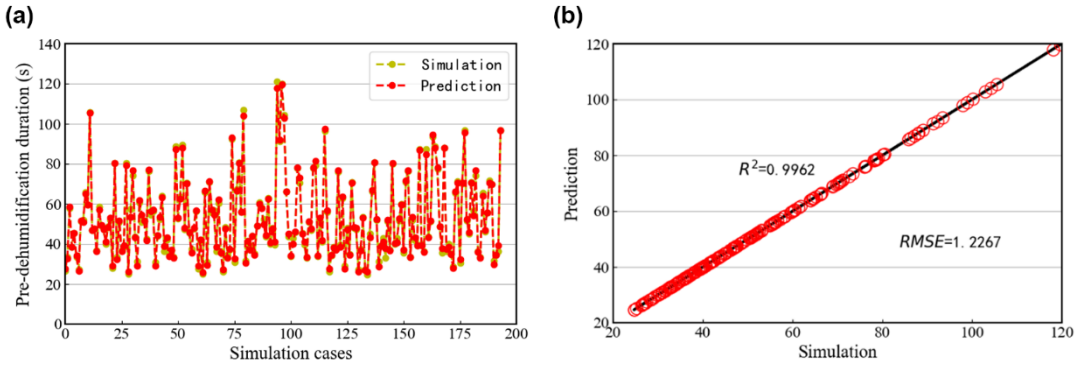

Figure 18. The training results of the pre-dehumidification duration: (a) the comparison and (b) the correlation of the predicted and simulated values.

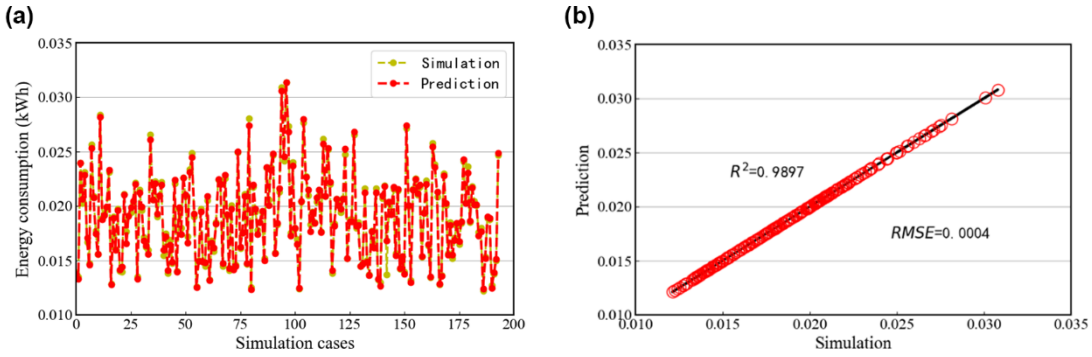

Figure 19. The training results of the pre-dehumidification energy consumption: (a) the comparison and (b) the correlation of the predicted and simulated values.

Validation results for the duration and energy consumption of pre-dehumidification

Through repeated training and the continuous debugging of the learning rate of the BP neural network, a well-trained model was obtained. The verification results of the data predicted by the trained prediction

model and the simulated data are presented as follows.

Figures 20 and 21 exhibit the validation results of the BP neural network for the duration and energy consumption of pre-dehumidification. The values predicted by the BP neural network had a high degree of fitting with the simulated values. The R^2 and RMSE values of the validation results for the pre-dehumidification duration were respectively 0.9916 and 1.6319, and those for the pre-dehumidification energy consumption were respectively 0.9872 and 0.0004. The R^2 values of the validation results were both high, indicating that the BP neural network can well reflect the internal relationships between the duration of the pre-dehumidification stage and the input variables, and is characterized by a strong nonlinear mapping ability and high prediction accuracy. The model with the best results was then saved for subsequent prediction analysis.

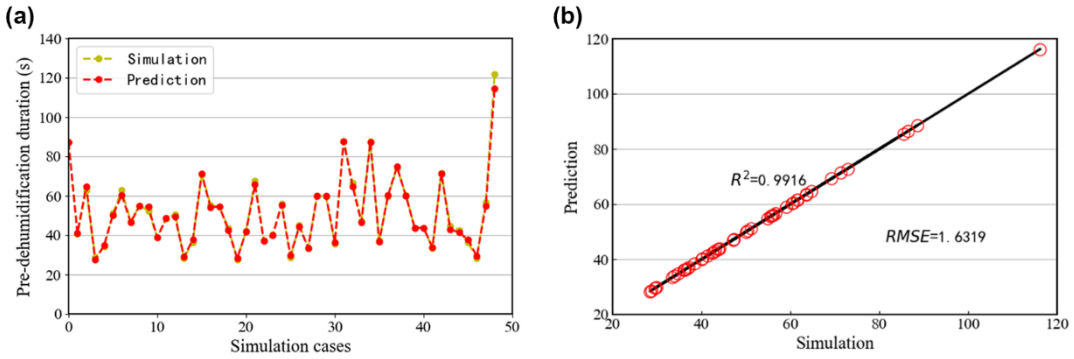

Figure 20. The validation results of the pre-dehumidification duration: (a) the comparison and (b) the correlation of the predicted and simulated values.

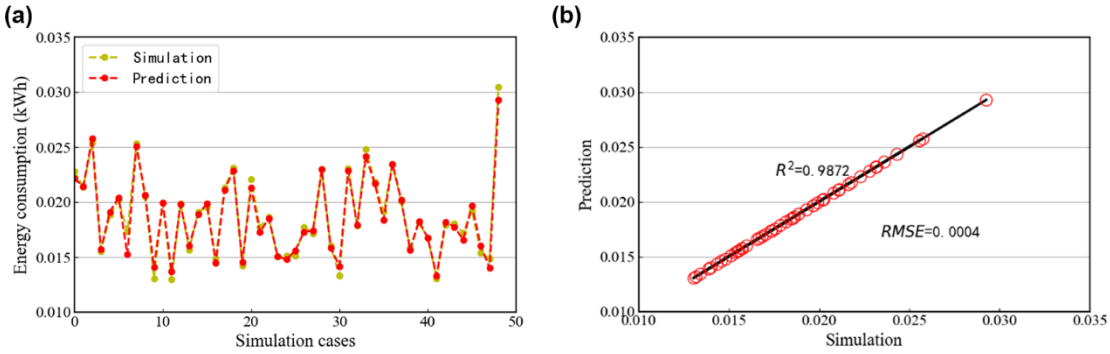

Figure 21. The validation results of the pre-dehumidification energy consumption: (a) the comparison and (b) the correlation of the predicted and simulated values.

Analysis results of BP neural network prediction

Prediction of simulation cases

All the effect factors of the input samples in the pre-dehumidification stage were taken as the new predictive input data and input into the trained BP neural network model. The predicted results were compared with the simulation results presented in Figures 22 and 23.

The values predicted by the BP neural network model were found to have a high degree of fitting with the simulated values, and the fitting lines almost completely overlapped. Thus, in future practical applications, the BP neural network can be used to accurately estimate the pre-dehumidification duration and energy consumption according to the running parameters of the indoor environment. The best pre-dehumidification duration will then be used as a signal that is transmitted to the fan. The fan will then run in advance after receiving the signal to prevent condensation on the floor.

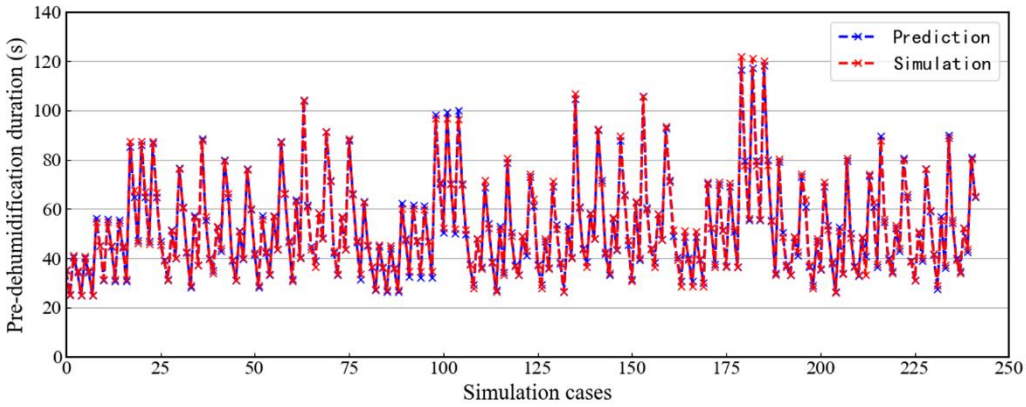

Figure 22. The comparison of the predicted and simulated values of the pre-dehumidification duration.

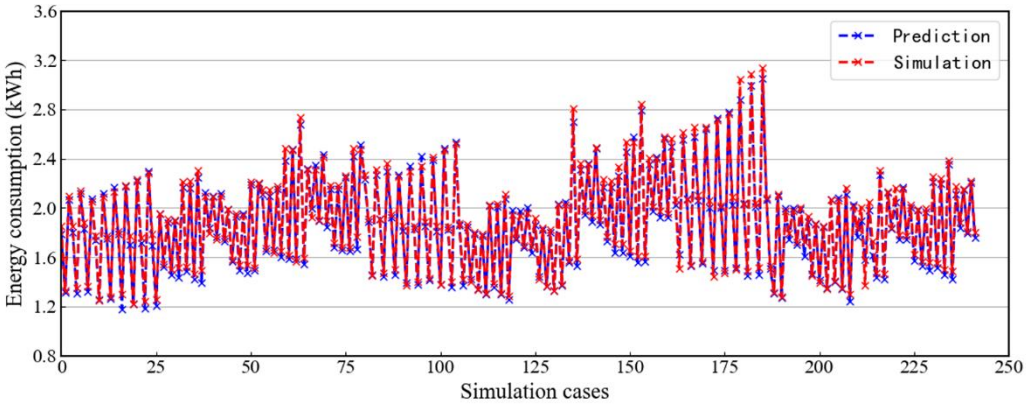

Figure 23. The comparison of the predicted and simulated values of the pre-dehumidification energy consumption.

Prediction results of the effects of the control factors

To determine the universal laws of the effects of the control factors on the pre-dehumidification duration and energy consumption, larger ranges of data were set based on the scopes of different parameters, as reported in Table 6. T_{ini} and H_{ini} are directly related to T_{ad}, and the dehumidifying period was designed to end when T_{ad} was lower than T_{floor} = 2°C. The difference between T_{floor} and T_{ad} has an important influence on the setting of the initial T_{ad}. Therefore, the difference ΔT between T_{floor} and T_{ad} was selected to represent the initial value of T_{ad} for different values of T_{floor}. The value ranges of the other parameters were in compliance with the values reported in boundary condition setting section. The data set was substituted into the trained BP neural network model for prediction, and the influences of different control parameters on the pre-dehumidification duration and energy consumption were obtained, as subsequently discussed.

Table 6. The data ranges for prediction.

Decision variables	Range	Unit
V_{as}	0.02-0.035	m^3/s
T_{as}	20-23	°C
H_{as}	7.25-11	g/kg
T_{floor}	21-24	°C
ΔT	0-1.5	°C

Figure 24(a) exhibits the three-dimensional diagram of variation trends of the pre-dehumidification duration with variations of T_{as} and H_{as}. T_{as} was varied from 20 to 23°C, and the other parameters remained constant. The pre-dehumidification duration increased with the increase in T_{as}. The blue histogram in Figure 25(a) presents the pre-dehumidification duration at different values of T_{as}. The variation of the pre-dehumidification duration with the variation in T_{as} was not obvious. With the increase in T_{as} by 0.2°C, the maximum pre-dehumidification duration was 0.27 s. With the increase in T_{as} from 20 to 23°C, the pre-dehumidification duration was increased from 43.9 to 44.97 s, a variation of only 2.38%. Moreover, with the increase in T_{as}, the air humidity ratio was increased, and the difference in the indoor air humidity ratio was reduced. Furthermore, the dehumidification speed became slow, and the effect of the humidity ratio on the

air dew point temperature was greater. Therefore, with the increase in T_{as}, the initial indoor T_{ad} took a long amount of time to reduce to the T_{floor} difference of 2°C. Hence, when T_{as} was increased, the pre-dehumidification duration would be increased, and vice versa.

As shown from the three-dimensional diagram in Figure 24(a), the pre-dehumidification duration exhibited an increasing trend with the increase of H_{as} under the condition of the other parameters remaining unchanged. The blue histogram in Figure 25(b) shows the pre-dehumidification duration at different values of H_{as}. With the variation of H_{as} from 7.25 to 11 g/kg, the pre-dehumidification duration was increased from 35.76 to 44.97 s, a variation of 20.5%. With the increase of H_{as}, the speed of the dehumidification became slow. Therefore, when H_{as} was increased, the pre-dehumidification duration would also be increased.

Figure 24(b) presents the three-dimensional diagram of the variation trends of the energy consumption with the variation of T_{as} and H_{as}. The energy consumption was found to decrease with an increase of T_{as} and a decrease of H_{as}. The red histogram in Figure 25(a) presents the energy consumption at different values of T_{as}. With the decrease in T_{as} from 23 to 20°C, the energy consumption was increased from 1.99 to 2.04 kWh, an increase of 2.4%. With the variation of T_{as}, the energy consumption was related to the pre-dehumidification duration and the difference in the enthalpy of the air supply and the outdoor air. The effect of T_{as} on the pre-dehumidification duration was found to be very small. Thus, the energy consumption was mainly dependent on the difference in the enthalpy of the air supply and the outdoor air. The greater the value of T_{as}, the smaller the difference in the enthalpy of the air supply and the outdoor air. Hence, if T_{as} was increased, the energy consumption would be decreased.

The red histogram in Figure 25(b) shows the energy consumption at different values of H_{as}. With the decrease in H_{as} by 0.25 g/kg, the energy consumption was decreased by 0.01 kWh. With the variation of the value of H_{as} from 11 to 7.25 g/kg, the energy consumption was decreased from 1.99 to 1.82 kWh. Because only the value of H_{as} was varied, the energy consumption was also related to the pre-dehumidification duration and the difference in the enthalpy of the air supply and the outdoor air. The variation of H_{as} was small, and the difference in the enthalpy of the air supply and the outdoor air was also small. Therefore, the decisive factor of energy consumption was found to be the pre-dehumidification duration. The smaller the value of H_{as}, the shorter the pre-dehumidification duration; thus, the energy consumption was also smaller.

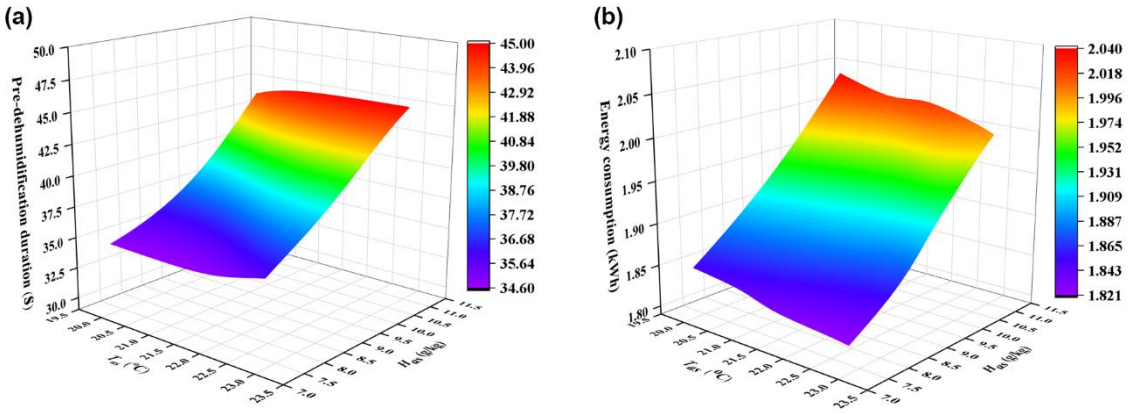

Figure 24. The three-dimensional diagram of the variation trends of the pre-dehumidification (a) duration and (b) energy consumption with the variations of T_{as} and H_{as}.

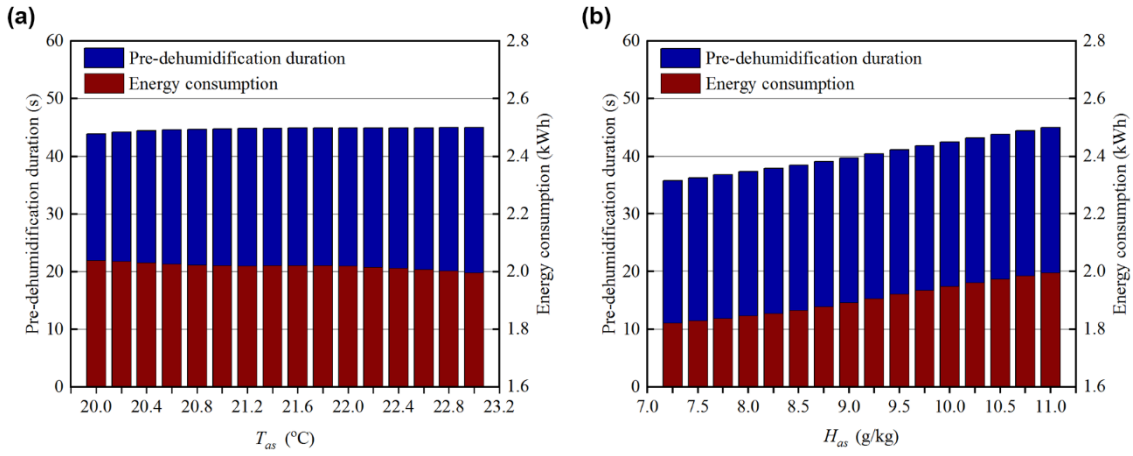

Figure 25. The pre-dehumidification duration and energy consumption at different values of (a) T_{as} and (b) H_{as}.

Figure 26(a) exhibits the three-dimensional diagram of variation trends of the pre-dehumidification duration with the variation of V_{as} and T_{floor}. The value of V_{as} varied from 0.02 to 0.035 m^3/s, and the other parameters were kept constant. The pre-dehumidification duration was decreased with an increase in V_{as}. The blue histogram in Figure 27(a) presents the pre-dehumidification duration at different values of V_{as}. With an increase in V_{as} from 0.02 to 0.035 m^3/s, the pre-dehumidification duration was decreased by 47.7%. With an increase in V_{as}, the dehumidification speed was increased, which allowed the indoor T_{ad} to be rapidly reduced to reach the target difference from the value of T_{floor}. Therefore, with the increase in V_{as}, the pre-dehumidification duration was increased. Furthermore, the value of V_{as} was found to have a significant effect on the pre-dehumidification duration. As shown from the three-dimensional diagram in Figure 26(a), the pre-dehumidification duration exhibited a decreasing trend with the increase in T_{floor} under the condition of other parameters remaining unchanged. The blue histogram shown in Figure 27(b) shows the pre-dehumidification duration at different values of T_{floor}. With the variation in T_{floor} from 21 to 24°C, the pre-dehumidification duration was varied from 93.98 to 51.25 s, which is a decrease of 45.4%. With the increase of T_{floor}, the set initial indoor T_{ad} was increased, which means that the humidity ratio of the indoor air was increased, resulting in the increase in the difference between the humidity ratio of the air supply and the indoor air, as well as the increase of the dehumidification rate. Therefore, with the increase in T_{floor}, the pre-dehumidification duration was decreased. Thus, V_{as} and T_{floor} were both found to have significant effects on the pre-dehumidification duration.

Figure 26(b) shows the three-dimensional diagram of the variation trends of the energy consumption with the variation in V_{as} and T_{floor}. The figure indicates that the energy consumption was decreased with the increase of T_{floor}. However, with the increase in V_{as}, the energy consumption exhibited a fluctuating trend. The red histogram in Figure 27(a) reveals the energy consumption at different values of V_{as}. With the increase in V_{as} from 0.02 to 0.026 m^3/s, the energy consumption was decreased by 2.7%; with the increase in V_{as} from 0.026 to 0.03 m^3/s, the energy consumption was increased by 8%; then, with the increase in V_{as} from 0.03 to 0.035 m^3/s, the energy consumption was decreased by 5.3%. In addition, the minimum energy consumption occurred with the variation in V_{as} in the range of 0.02 to 0.03 m^3/s; when V_{as} = 0.026 m^3/s, the energy consumption was 1.78 kWh. This indicates that the effect of V_{as} on the energy consumption was not significant, and a minimum energy consumption value would occur within a certain range of the variation in V_{as}.

The red histogram in Figure 27(b) displays the energy consumption at different values of T_{floor}. With the increase in T_{floor} from 20 to 24°C, the energy consumption was decreased from 3.02 to 1.83 kWh, a decrease of 39.4%. With the variation in T_{floor}, the energy consumption was dependent only on the pre-dehumidification duration. With the increase in T_{floor}, the pre-dehumidification duration was decreased, and the energy consumption was gradually decreased.

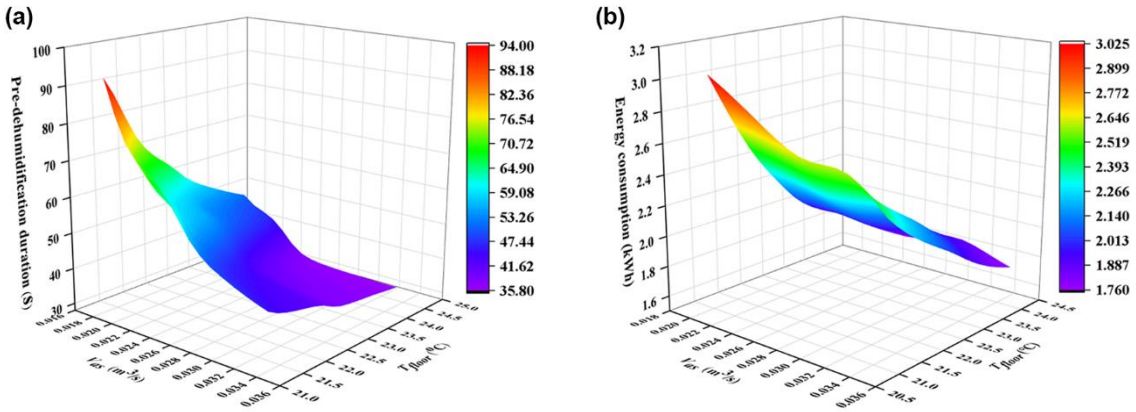

Figure 26. The three-dimensional diagrams of the variation trends of the pre-dehumidification (a) duration and (b) energy consumption with the variations in V_{as} and T_{floor}.

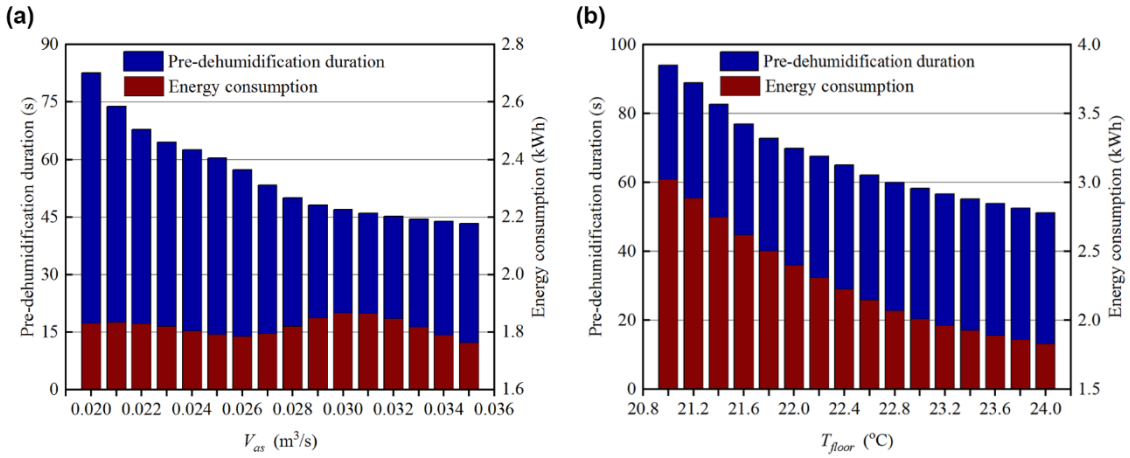

Figure 27. The pre-dehumidification duration and energy consumption at different values of (a) V_{as} and (b) T_{floor}.

Figure 28(a) displays the three-dimensional diagram of the variation trend of the pre-dehumidification duration with a variation in T_{ad}. ΔT was used to represent the corresponding initial indoor T_{ad} under different values of T_{floor}. The pre-dehumidification duration was decreased with an increase in ΔT; this means that as the initial T_{ad} was decreased, the pre-dehumidification duration was decreased. The value of ΔT was varied from 0 to 1.5°C. The blue histogram in Figure 29 shows the pre-dehumidification duration at different values of ΔT. With an increase in ΔT by 0.1°C, the pre-dehumidification duration was shortened by about 3 s. Moreover, with an increase in ΔT from 0 to 1.5°C, the pre-dehumidification duration was shortened from 71.2 to 29.11 s, a decrease of 59.1%. As the difference was increased, the value of T_{ad} was decreased. This means that the humidity ratio of the indoor air was decreased and the dehumidification rate was increased. Thus, the pre-dehumidification duration was gradually decreased with an increase in ΔT.

Figure 28(b) exhibits the three-dimensional diagram of the variation trend in the energy consumption with a variation in T_{ad}, which indicates that the energy consumption was decreased with an increase in ΔT. The red histogram in Figure 29 presents the energy consumption at different values of ΔT. With an increase in ΔT from 0 to 1.5°C, the energy consumption was decreased from 1.83 to 1.02 kWh, a decrease of 44.2%. With a variation in the initial indoor T_{ad}, the energy consumption was dependent only on the pre-dehumidification duration. With a decrease in T_{ad}, the pre-dehumidification duration was decreased; thus, the energy consumption also was decreased. Therefore, based on the preceding analysis, T_{ad} had the most significant effect on the pre-dehumidification duration and energy consumption.

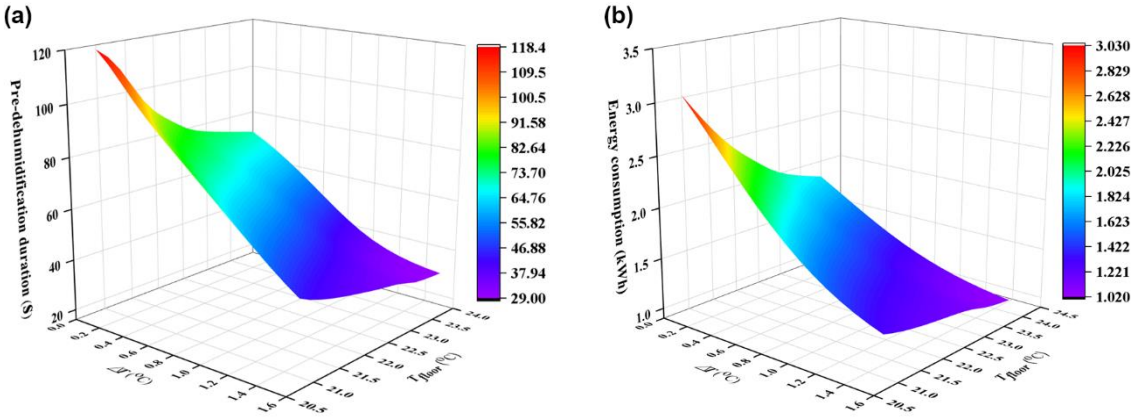

Figure 28. The three-dimensional diagrams of the variation trends of the pre-dehumidification (a) duration and (b) energy consumption with a variation in ΔT.

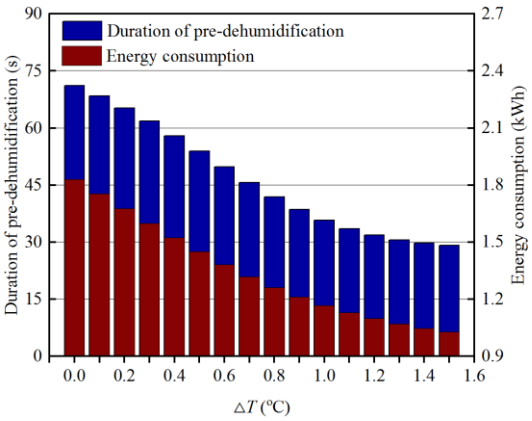

Figure 29. The pre-dehumidification duration and energy consumption at different values of *ΔT*.

Discussion

In view of the pre-dehumidification problem, a CFD model of a typical office room with RFC and a DV system was constructed. Typical working cases with different initial indoor conditions and air supply parameters were considered in this study. The standard for the end of the pre-dehumidification stage was whether the difference between the dew point temperature of the air near the floor and the floor temperature reached 2°C. Therefore, the duration of the pre-dehumidification of the air supply system was determined, and the energy consumption was calculated according to Equations (12) and (13). Because the CFD simulation required a substantial amount of calculation time, the shortening of which is a strict requirement for the computer, a BP neural network prediction model was established and trained based on the sample data set. Finally, the CFD simulation was replaced by the trained BP neural network prediction model, which provided a novel and effective method for the control of pre-dehumidification. In summary, compared to similar research, the unique advantage of this study is that CFD simulation was combined with a BP neural network. This method can predict the detailed situation of the indoor air distribution and the duration. The energy consumption of pre-dehumidification can also be quickly predicted according to different initial conditions.

While this study provided a novel and effective evaluation method for RFC pre-dehumidification control, it was characterized by some limitations for practical engineering applications. For example, the influences of only five factors on the duration and the energy consumption of pre-dehumidification were analyzed, and only a typical office was chosen for the study of thermal performance and variations in temperature and humidity. Therefore, the established prediction model can only be used in a specific situation. Although the energy consumption of the whole building was assessed, it was only the result of multiplication on the basis of the room studied. In reality, the energy consumption would vary according to the size and function of the room. Questions about the space of the heat transfer and energy use have not been successfully addressed via the use of CFD technology. Thus, based on previous studies, Equations (12) and (13) were established. However, the energy consumption of the chiller and other equipment that was used to meet the requirements of the cooling load was ignored in the calculation process.[47] Thus, the calculation of energy consumption was not carried out comprehensively. Different sizes of the air supply inlet and different ventilation methods (mixed ventilation, stratum ventilation and underfloor ventilation) could affect the duration and energy consumption of pre-dehumidification to a certain extent. Therefore, the established BP neural network prediction model has certain limitations, and further research would be needed to consider the influencing factors more comprehensively.

In addition, the simulated data were divided into two parts; 80% was used for BP neural network training, and 20% was used for forecasting model validation. However, the data set was small and contained only 243 data sets. In follow-up research, more influencing factors should be considered to set up more simulation conditions, which will be used to expand the BP neural network training data set. Thus, the universality of the prediction model can be improved.

Regarding the variation of the floor temperature, the floor was assumed as a constant-temperature surface in this study. Previous studies have shown that RFC systems have thermal inert,[59,60] and that the floor temperature would vary due to variations in the water supply temperature and flow rate. Building thermal inertia is a complex phenomenon that depends on the time-varying characteristics of heat transfer and heat flows. From this perspective, transient external climatic conditions, such as the outdoor air temperature and solar radiation, have important impacts on the thermal performance of RFC systems due to

the effect of thermal inertia.[61] In other words, via the investigation of the thermal mass of a building envelope, overheating risks induced by the time-varying outdoor air temperature can be delayed or reduced, thereby preventing the thermal discomfort of the building occupants.[62]

Therefore, further studies must consider this influencing factor. Moreover, the simulation speed can be improved by dimensionality reduction calculation.[63] For example, the proper orthogonal decomposition (POD) calculation method[64] can reduce the dimension of differential equations. Within a certain precision loss range, fast calculation and prediction can be realized, thereby reducing the calculation load and shortening the calculation time. Finally, future work will be carried out in a self-built laboratory to control the indoor thermal environment,[65] and to better illustrate the universality and feasibility of the established prediction model. The ultimate objective is to achieve a more practical control and provide a reliable reference for the operation control of the composite system.

Conclusion

In this study, the combination of CFD simulation and BP neural network prediction was adopted to investigate the effects of T_{as}, V_{as}, H_{as}, T_{floor} and T_{ini} and H_{ini} on the pre-dehumidification stage in RFC and DV systems. The conclusions of this research are as follows.

The BP neural network validation results demonstrated that the R^2 values of the training and validation results were very high, and respectively reached 0.99 and 0.98. These findings indicate that the BP neural network model established in this study can be used for the prediction of moisture condensation risk on the surface of the RFC system.

The results predicted by the BP neural network revealed that decreasing the initial T_{ad} can effectively shorten the pre-dehumidification duration and the energy consumption. With an increase in ΔT from 0 to 1.5°C, the pre-dehumidification duration was shortened from 71.2 to 29.11 s, a decrease of 59.1%, and the energy consumption was decreased by 44.2%. Furthermore, the effect of T_{as} on the pre-dehumidification duration was not found to be significant. With a variation in V_{as}, the energy consumption fluctuated. Thus, increasing the value of V_{as} was found to have no significant effect.

CRediT author statement

Meng Su: Software, Data curation, Writing - Original Draft, Formal analysis, Visualization. Jiying Liu: Conceptualization, Methodology, Supervision, Writing - Review & Editing, Project administration, Funding acquisition. Shiyu Zhou: Writing- Reviewing and Editing, Visualization. Jikun Miao: Writing-Reviewing and Editing, Project administration, Funding acquisition. Moon Keun Kim: Writing-Reviewing and Editing.

Declaration of competing interest

The authors declare no potential conflicts of interest with respect to the research, authorship, and/or publication of this article.

Acknowledgements

This work was funded by Natural Science Foundation of Shandong Province (ZR2021ME199) and Key Research and Development Project in Shandong Province (2018GSF121003). This work was also supported by the Plan of Introduction and Cultivation for Young Innovative Talents in Colleges and Universities of Shandong Province.

References

1.Li X, Yu CWF. China's Building Energy Efficiency Targets: Challenges or Opportunities? *Indoor Built Environ* 2012; 21(5): 609-613. http://doi.org/10.1177/1420326x12460463.

2.Rhee KN, Kim KW. A 50 year review of basic and applied research in radiant heating and cooling systems for the built environment. *Build Environ* 2015; 91: 166-190. http://doi.org/10.1016/j.buildenv.2015.03.040.

3.Kim JT, Yu CWF. Sustainable Development and Requirements for Energy Efficiency in Buildings - The Korean Perspectives. *Indoor Built Environ* 2018; 27(6): 734-751. http://doi.org/10.1177/1420326x18764618.

4.Zhao M, Kang WB, Luo XL, Yu CWF, Meng XZ, Gu ZL. Performance comparison of capillary mat radiant and floor radiant heating systems assisted by air source heat pump in residential buildings. *Indoor Built Environ* 2017; 26(9): 1292-1304. http://doi.org/10.1177/1420326x16674517.

5.Su J, Li J, Luo X, Yu CW, Gu Z. Experimental evaluation of a capillary heating bed driven by an air source

heat pump and solar energy. *Indoor Built Environ* 2020; 29(10): 1399-1411. http://doi.org/10.1177/1420326x19878576.
6.Xie D, Tian L, Liao ML, Yu CW, Wang HQ. The thermal environment of non-steady state radiation heat transfer with a capillary ceiling radiation cooling system. *Indoor Built Environ* 2019; 28(4): 443-453. http://doi.org/10.1177/1420326x18804012.
7.Xie D, Wang C, Yu CW, Wang H. Performance of capillary ceiling cooling panel on ceiling surface temperature and indoor thermal environment. *Indoor Built Environ* 2020; 29(6): 881-894. http://doi.org/10.1177/1420326x20917740.
8.Kim MK, Liu J, Cao S-J. Energy analysis of a hybrid radiant cooling system under hot and humid climates: a case study at Shanghai in China. *Build Environ* 2018; 137: 208-214. http://doi.org/10.1016/j.buildenv.2018.04.006.
9.Liu J, Li Z, Kim MK, Zhu S, Zhang L, Srebric J. A comparison of the thermal comfort performances of a radiation floor cooling system when combined with a range of ventilation systems. *Indoor Built Environ* 2020; 29(4): 527-542. http://doi.org/10.1177/1420326X19869412.
10.Li H, Gong G, Xu C, Su H, Cao Z, Zhou M, Yu CWF. Thermal and Humid Environment and Moisture Condensation Characteristics of Cold Surfaces. *Indoor Built Environ* 2014; 23(3): 474-484. http://doi.org/10.1177/1420326X19869412.
11.Tang H, Liu X-H, Li H, Zhou Y, Jiang Y. Study on the reduction of condensation risks on the radiant cooling ceiling with superhydrophobic treatment. *Build Environ* 2016; 100: 135-144. http://doi.org/10.1016/j.buildenv.2016.02.008.
12.Zhong Z, Niu J, Ma W, Yao S, Yang M, Wang Z. An experimental study of condensation on an aluminum radiant ceiling panel surface with superhydrophobic treatment. *Energy Build* 2021; 252: 111393. http://doi.org/10.1016/j.enbuild.2021.111393.
13.Xing D, Li N, Cui H, Zhou L, Liu Q. Theoretical study of infrared transparent cover preventing condensation on indoor radiant cooling surfaces. *Energy* 2020; 201: 117694. http://doi.org/10.1016/j.enery.2020.117694.
14.Guo S, Tian Y, Fan D, Wu W, Zhao J, Jin G. A novel operating strategy to avoid dew condensation for displacement ventilation and chilled ceiling system. *Appl Therm Eng* 2020; 176: 115344. http://doi.org/10.1016/j.applthermaleng.2020.115344.
15.Jin W, Ma J, Jia L, Wang Z. Dynamic Variation of Surface Temperatures on the Radiant Ceiling Cooling Panel based on the Different Supply Water Temperature Adjustments. *Sustain Cities and Soc* 2020; 52: 101805. https://doi.org/10.1016/j.scs.2019.101805.
16.Song D, Kim T, Song S, Hwang S, Leigh SB. Performance evaluation of a radiant floor cooling system integrated with dehumidified ventilation. *Appl Therm Eng* 2008; 28: 1299-1311.
17.Lim H, Kang YK, Jeong JW. Application of a phase change material to a thermoelectric ceiling radiant cooling panel as a heat storage layer. *J Build Eng* 2020; 32: 101787. https://doi.org/10.1016/j.jobe.2020.101787.
18.Zhong Z, Niu J, Ma S, Yao S, Yang M, Wang Z. An experimental study of condensation on an aluminum radiant ceiling panel surface with superhydrophobic treatment. *Energy Build* 2021; 252(7734): 111393. https://doi.org/10.1016/j.enbuild.2021.111393.
19.Fauchoux M, Bansal M, Talukdar P, Simonson CJ, Torvi D. Testing and modelling of a novel ceiling panel for maintaining space relative humidity by moisture transfer. *Int J Heat Mass Transf* 2010; (19/20): 3961-3968. https://doi.org/10.1016/ j.ijheatmasstransfer.2010.05.015.
20.Xie D, Tian L, Yu CW, Liao M, Wang H. Indoor thermal environment due to non-steady-state radiation heat transfer of a capillary ceiling radiation cooling system. *Indoor Built Environ* 2019; 29(4): 443-453. https://doi.org/10.1177/1420326X18804012.
21.Karacavus B, Aydin K. Numerical investigation of general and local thermal comfort of an office equipped with radiant panels. *Indoor Built Environ* 2019; 28(6): 208-214. https://doi.org/10.1177/1420326X18799834.
22.Kim MK, Liu J, Cao S-J. Energy analysis of a hybrid radiant cooling system under hot and humid climates: a case study at Shanghai in China. *Build Environ* 2018; 137: 208-214. https://doi.org/10.1016/j.buildenv.2018.04.006.
23.Feng J, Schiavon S, Bauman F. New method for the design of radiant floor cooling systems with solar radiation. *Energy Build* 2016; 125: 9-18. https://doi.org/10.1016/j.enbuild.2016.04.048.
24.Tang H, Liu X-H, Jiang Y. Theoretical and experimental study of condensation rates on radiant cooling surfaces in humid air. *Build Environ* 2016; 97(15): 1-10. https://doi.org/10.1016/j.buildenv.2015.12.003.

25.Lim J-H, Jo J-H, Kim Y-Y, Yeo MS, Kim KW. Applieation of the control methods for radiant floor cooling system in residential buildings. *Build Environ* 2006; 41(1): 60-73. https://doi.org/10.1016/j.buildenv.2005.01.019.
26.Jeong C, Yeo M. Feasibility of a Radiant Floor Cooling System for Residential Buildings with Massive Concrete Slab in a Hot and Humid Climate. *Int J Concr Struct M* 2018; 12(1): 3-14. https://doi.org/10.1186s40069-018-0314-z.
27.Wilkins C, Kosonen R. Cool ceiling system: a European air-conditioning alternative. *ASHRAE J* 1992; 34: 41-45. https://doi.org/10.1080/02786829208959564.
28.Zong J, Liu J, Ai Z, Kim MK. A review of human thermal plume and its influence on the inhalation exposure to particulate matter. *Indoor Built Environ* 2022. https://doi.org/ 10.1177/1420326X221080358 .
29.Engelmana P, Kalz D, Salvalai G. A review of CFD analysis methods for personalized ventilation (PV) in indoor built environments. *Sustainability* 2019; 11(15): 4166. https://doi.org/10.3390/su11154166 .
30.Zhang C, pomianowski M, Heiselberg PK. A review of integrated radiant heating/cooling with ventilation systems-Thermal comfort and indoor air quality. *Energy Build* 2020; 223: 110094. https://doi.org/10.1016/j.enbuild.2020.1 10094.
31.Awbi HB. Energy efficient room air distribution. *Renew Energy* 1998; 15: 293-299. https://doi.org/10.1016/S0960-1481(98)00176-1.
32.Xing H, Hatton A, Awbi HB. A study of the air quality in the breathing zone in a room with displacement ventilation. *Build Environ* 2001; 36: 809-820. https://doi.org/10.1016/S0360-1323(01)00006-3.
33.Ren J, Liu J, Zhou S, Kim MK, Song S. Experimental study on control strategies of radiant floor cooling system with direct-ground cooling source and displacement ventilation system: A case study in an office building. *Energy* 2022; 239(15): 122410. https://doi.org/10.1016/j.energy.2021.122410.
34.Liu J, Kim MK, Srebric J. Numerical analysis of cooling potential and indoor thermal comfort with a novel hybrid radiant cooling system in hot and humid climates. *Indoor Built Environ* 2022; 31(4): 929-943. https://doi.org/10.1177/1420326x211040853.
35.Liu J, Dalgo D, Zhu S, Li H, Zhang L, Srebric J. Performance analysis of a ductless personalized ventilation combined with radiant floor cooling system and displacement ventilation. *Build Simul* 2019; 12(5): 905-919. https://doi.org/10.1007/s12273-019-0521-9.
36.Nasruddin, Sholahudin, Satrio P, Mahlia TMI, Giannetti N, Saito K. Optimization of HVAC system energy consumption in a building using artificial neural network and multi-objective genetic algorithm. Sustain. *Energy Technol Assess* 2019; 35: 48-57. https://doi.org/10.1016/j.seta.2019.06.002.
37.Sholahudin S, Han H. Heating load predictions using the static neural networks method. *Int J Technol* 2015; 6(6): 946-953. https://doi.org/10.14716/ijtech.v6i6.1902.
38.Mba L, Meukam P, Kemajou A. Application of artificial neural network for predicting hourly indoor air temperature and relative humidity in modern building in humid region. *Energy Build* 2016; 121: 32-42. https://doi.org/10.1016/j.enbuild.2016.03.046.
39.Zhao R. Concise air conditioning design manual. Beijing: China Architecture & Building press, 1998.
40.Cengel TMY. A Practical Approach, Mc-Graw Hill Education, Columbus, GA, USA. 2003.
41.Chen Q. Comparison of different k-ε models for indoor air flow computations. *Numer Heat Tr B-fund* 1998; 28(3): 353-369. https://doi.org/10.1080/10407799508928838.
42.Davidson L. An Introduction to Turbulence Models. Goteborg, Sweden: Chalmers University of Technology, 2018.
43. GB 50365-2019. Ministry of Housing and Urban-Rural Development of the People's Republic of China (MOHURD). Standard for operation and management of central air conditioning system. Beijing: China Architecture & Building press, 2019.
44.Skistad H, Mundt E, Nielsen PV, Hagstrom K, Ralio J. Displacement ventilation in non-industrial premises. Brussels, Belgium: Rehva Guidebook No. 1, 2002.
45.Olesen B. Radiant floor cooling systems. *ASHRAE J* 2008. https://doi.org/10.1002/stc.237.
46.Zhang C, Pomianowski M, Heiselberg PK, Yu T. A review of integrated radiant heating/cooling with ventilation systems- Thermal comfort and indoor air quality. *Energy Build* 2020; 223(15): 110094. https://doi.org/10.1016/j.enbuild.2020.110094.
47.Xu HT, Niu JL. Numerical procedure for predicting annual energy consumption of the under-floor air distribution system. *Energy Build* 2006; 38:641-647. https://doi.org/10.1016/j.enbuild.2005.10.003.
48. JGJ/T 449-2018. Ministry of Housing and Urban-Rural Development of the People's Republic of China (MOHURD). Standard for green performance calculation of civil buildings. Beijing: China Architecture & Building press, 2018.

49.Zhang T, Hari Q, Zhao Q. The use of the interval pareto sorting method in simulation-based design of an indoor environment. *Sci Technol Built En* 2018; 24: 410-417. https://doi.org/10.1080/23744731.2017.1394142.
50.Zhou L, Haghighat F. Optimization of ventilation system design and operation in office environment, Part I: Methodology. *Build Environ* 2009; 44: 651-656. https://doi:10.1016/j.buildenv.2008.05.009.
51.Xu Y, Yang X, Yang C, Srebric J. Contaminant dispersion with personal displacement ventilation Part I: Base case study. *Buid Environ* 2009; 44(10): 2121-2128. https://doi.org/10.1016/j.buildenv.2009.03.006.
52.Ma X, Li X, Shao X, Jiang X. An algorithm to predict the transient moisture distribution for wall condensation under a steady flow field. *Buid Environ* 2013; 67: 56-58. https://doi.org/10.1016/j.buildenv.2013.04.028.
53.Nasruddin, Sholahudin, Satrio P, Mashlia TMI, Giannetti N, Saito K. Optimization of HVAC system energy consumption in a building using artificial neural network and multi-objective genetic algorithm. Sustain. *Energy Technol Assess* 2019; 35: 48-57. https://doi.org/10.1016/j.seta.2019.06.002.
54.Said SAM. Degree-day base temperature for residential building energy prediction in Saudia Arabia. *ASHRAE Trans Res* 1992; 98(1): 346-353.
55.Imran T, Shafiqur R, Khaled B. Application of neural networks for the prediction of hourly mean surface temperatures in Saudi Arabia. *Renew Energ* 2002; 35(4): 545-554. https://doi.org/10.1016/S0960-1481(01)00082-9.
56.Ren L, Liu Y, Rui Z. Application of Elman Neural Network and MATLAB to Load Forecasting. In: *International conference on information technology and computer science* 04 August 2009, pp. 55-59. https://doi.org/10.1109/ITCS.2009.20.
57.Mohanraj M, Jayaraj S and Muraleedharan C. Applications of artificial neural networks for refrigeration, air-conditioning and heat pump systems—a review. *Renew Sustain Energy Rev* 2012; 16(2): 1340-1358. https://doi.org/10.1016/j.rser.2011.10.015.
58.Qi A. Research on Prediction Model of Improved BP Neural Network Optimized by Genetic Algorithm. In: *4th International Conference on Machinery, Materials and Computer* 2017, Shanxi: Xian, 27-29 November 2017. https://doi.org/ 10.2991/macmc-17.2018.145.
59.Zhao K, Liu X-H, Jiang Y. Dynamic performance of water-based radiant floors during start-up and high-intensity solar radiation. *Sol Energy* 2014; 101: 232-244. https://doi.org/10.1016/j.solener.2013.12.033.
60.Verbeke S, Audenaert A. Thermal inertia in buildings: a review of impacts across climate and building use. *Renew Sustain Energy Rev* 2018; 82: 2300-2318. https://doi.org/10.1016/j.rser.2017.08.083.
61.Chen YT. Application of adaptive predictive control to a floor heating system with a large thermal lag. *Energy Build* 2002; 34(01): 45-51. https://doi.org/10.1016/S0378-7788(01)00076-7.
62.Liu D, Zhou H, Hu A, Zhang Q, Liu N, Wen J. Study on the intermittent operation mode characteristic of a convection-radiation combined cooling system in office buildings. *Energy Build* 2022; 255: 111669. https://doi.org/10.1016/j.enbuild.2021.111669.
63.Chen Q, Li N. Fast simulation and high-fidelity reduced-order model of the multi-zone radiant floor system for efficient application to model predictive control. *Energy Build* 2021; 248: 111210. https://doi.org/10.1016/j.enbuild.2021.111210.
64.Du J, Fang F, Pain CC, Navon IM, Zhu J, Ham DA. POD Reduced-Order Unstructured Mesh Modeling Applied To 2D and 3D Fluid Flow. *Comput Math Appl* 2013; 65(3): 362-379. https://doi.org/10.1016/j.camwa.2012.06.009.
65.Zhu X, Liu J, Zhu X, Wang X, Du Y, Miao J. Experimental Study on Operating Characteristic of a Combined Radiant Floor and Fan Coil Cooling System in a High Humidity Environment. *Buildings* 2022; 12(4): 499. https://www.mdpi.com/2075-5309/12/4/499.